GRIND HARDENDING

OF

AISI 1045 AND AISI 52100 STEELS

To my wife Shazleen

and to Ammy and Aaron,

two wonderful kids who have enriched my life
more than I could imagine

GRIND HARDENING
OF
AISI 1045 AND AISI 52100 STEELS

By

RAZI SOHAIL

A Thesis
Submitted to the School of Graduate Studies
in Partial Fulfilment of the Requirements
for the Degree
Master of Applied Science

McMaster University

MASTER OF APPLIED SCIENCE (2006) McMaster University

(Mechanical Engineering) Hamilton, Ontario

TITLE:	Grind Hardening of AISI 1045 and AISI 52100 Steels
AUTHOR:	Razi Sohail
SUPERVISORS:	Dr. Philip Koshy & Dr. Mohamed Hamed
NUMBER OF PAGES:	xii, 92

Abstract

Case hardening of steels is extensively used throughout general engineering to produce components with a hardened layer whilst retaining a tough core. This is usually accomplished using different sources of energy, e.g. flame and induction being the most common. In recent years, a new case hardening technology, named 'Grind-Hardening' has surfaced. In this method, the heat dissipated during grinding is utilized to induce martensitic phase transformation in the surface layer of a component. Therefore it is possible to incorporate grinding and surface hardening into a single operation to develop a cost-effective production method. The grinding process then becomes an integrated heat treatment process.

In the present study on 'grind hardening', a numerical thermal model has been developed to compute the temperature distribution beneath the ground surface to predict the extent of surface hardening and the case depth. Grinding experiments were conducted in order to examine the influence of various process variables such as wheel depth of cut, feed speed, and wheel preparation. AISI 52100 and 1045 steels were used in this study to evaluate the behavior of plain and alloy steels during grind hardening. Effective case depth was measured using a Vickers hardness tester and was found to be over 0.5 mm for a target hardness of 513 Hv. Microstructure was analyzed using optical and scanning electron microscopes. The microstructure was observed to have fine martensitic laths which give rise to remarkable high hardness.

Acknowledgements

The work of this thesis has been an inspiring, often exciting, sometimes challenging, but always an interesting experience. It has been made possible by many people who have supported me.

First of all I would like to express my sincere gratitude to Dr. Philip Koshy for his patient guidance, encouragement and excellent advice through this study. My sincere thanks also goes to my co-supervisor Dr. Mohamed Hamed for his invaluable encouragement and guidance. I would like to convey my gratitude to Mr. Warren Reynolds for his technical support in the performance of grinding tests. Thankfulness is also due to Mr. Chris Butcher for his help on sample preparation and optical microscopy, Mr. Steve Koprich for his technical help on the Scanning Electron Microscope.

I am thankful to the Management of Niagara Machine Products (NMP) & Materials and Manufacturing Ontario (MMO) for their financial support; especially I feel indebted to Mr. Kelvin Lynch, Mr. Sean Kieffer and Mr. Ross Cappa of NMP and Mr. Harvey Pellegrini (MMO) for their support & encouragement in the completion of this project.

Finally, I take this opportunity to express my profound gratitude to my beloved wife and children for their moral support, love and patience during my study at McMaster.

Hamilton, Ontario

December 2006 Razi Sohail

Contents

List of Figures

List of Tables

Chapter 1

Introduction

The process route for case hardened engineering components, in general, entails rough machining in the soft state, followed by heat treatment and subsequent finish grinding. This represents an inefficient workflow in terms of logistics, and it is hence desirable to integrate the heat treatment phase into the machining process cycle. This is quite realistic considering that in a grinding process, essentially all of the energy is converted into heat at the grinding zone, of which a substantial proportion (typically 60-80%) is partitioned to the workpiece when using conventional aluminum oxide abrasives; the maximum temperature in the work material can therefore attain values exceeding the upper critical temperature [1], paving the way for the generation of a surface with the attributes of the requisite case hardness, surface finish and dimensional/form tolerances.

The proof-of-concept of such an innovative process termed "Grind-Hardening" has recently been established [2-7]. Case depths on the order of 1 mm have been achieved in AISI 52100 and AISI 4140 steels through martensitic phase transformation by short time austenitization of the surface layer, followed by self-quenching, in dry grinding. The generated surfaces have been demonstrated to comprise compressive

residual stresses and be devoid of surface cracks. The advantages of this novel process are two-fold:

i. Integration of the heat treatment phase into the production flow cycle results in improved material handling leading to a significant reduction in manufacturing lead time and cost, and

ii. Benefits to the environment arising from efficient energy utilization, and elimination of an energy intensive heat treatment process and the associated emissions.

The process can be accomplished on standard grinding equipment and does not necessitate any additional capital investment. Figure 1.1 shows a comparison of the production cycle with Grind Hardening to that with conventional heat treatment.

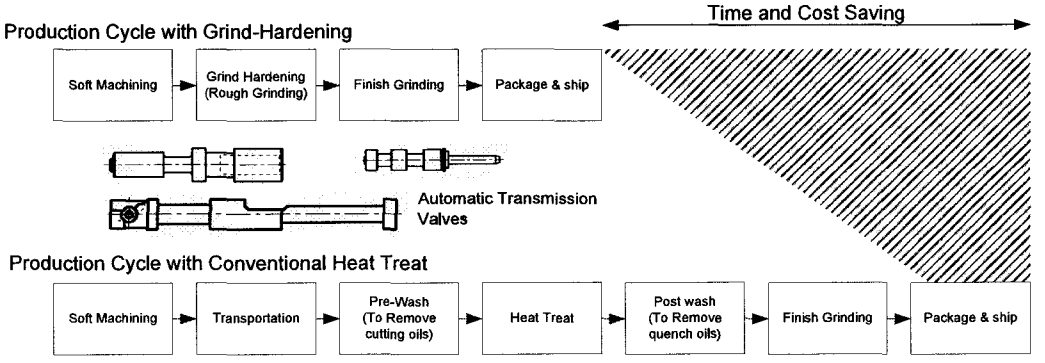

Figure 1.1 Comparison of conventional and integrated production sequences.

1.1 Background

Unlike in conventional machining by cutting, where much of the heat generated is transported in the chip (approx. 80%), in grinding most of the heat generated

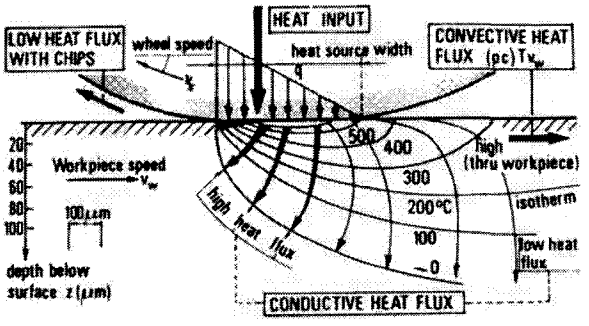

Figure 1.2 Schematic representation of isotherms in surface grinding process [13].

is conducted into the work material as shown in Figure 1.2. This complicated thermomechanical process has attracted extensive attention and research efforts over the part decades. The main concern of grinding processes has been the detrimental effects of high temperatures on the workpiece.

Many researchers investigated the dissipation of heat in grinding and the resulting influence on workpiece properties. The aim of most investigations was the prediction of undesirable alteration in the surface layer like cracks, tempered zones or white etching areas (WEA). These effects have been known for a long time and were perhaps first investigated and discussed by Tarasov [8] and Field and Kahles [9]. Later, this work was continued by Tonshoff, Konig, Malkin and other scientists [10-14]. Malkin and Fedoseev [15] first presented a model that considered material transformations derived from their characteristic time-temperature-transformation (TTT) diagram into account. Shaw and Vyas [16, 17] presented a theoretical treatment of metallurgical damage in ground surfaces.

Thermal damage is both academically intriguing and technologically significant, especially during tool grinding. Care is hence taken during grinding to accomplish required application properties. If process temperatures are too high but below the upper critical temperature line, it may temper the surface and reduce the surface hardness undermining the wear resistance of the tool surface due to lower hardness.

Figure 1.3 shows the hardness profile of a AISI 52100 bearing steel ground with light temper colors. Tempering has occurred at the surface which has softened the surface.

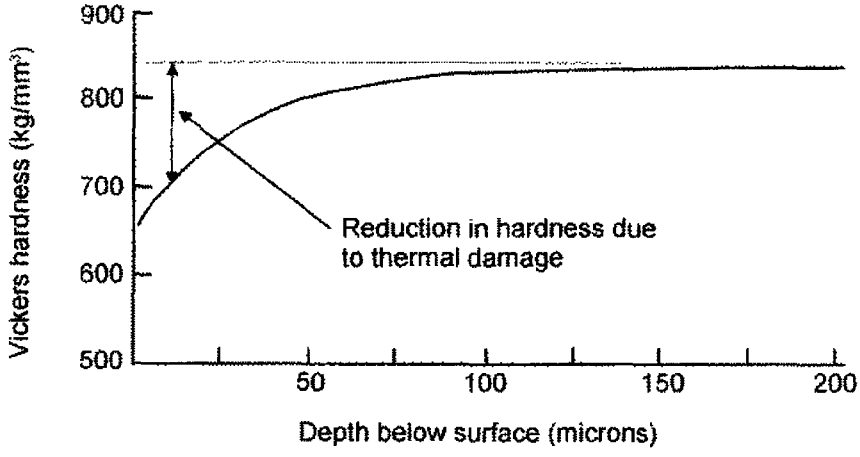

Figure 1.3 Microhardness variation below the workpiece surface caused by temper burn [18].

In cases where the surface temperature reaches values above the austenitizing temperature, researchers [13, 15, 19] have observed material transformation to martensite. The material cools rapidly after grinding due to the low temperature of the bulk material below the surface. This causes rehardening of the surface. AISI 52100 steel ground under abusive grinding conditions leading to rehardening is shown in Figure 1.4.

It is hence desirable to either dissipate grinding heat or utilize it effectively. It is well known that the temperature during grinding reaches above upper critical temperature line (Ac_3) leading to diffusion and phase transformation. Researchers [2, 3] have utilized this phenomenon to surface harden parts by utilizing the grinding heat by controlling the grinding parameters.

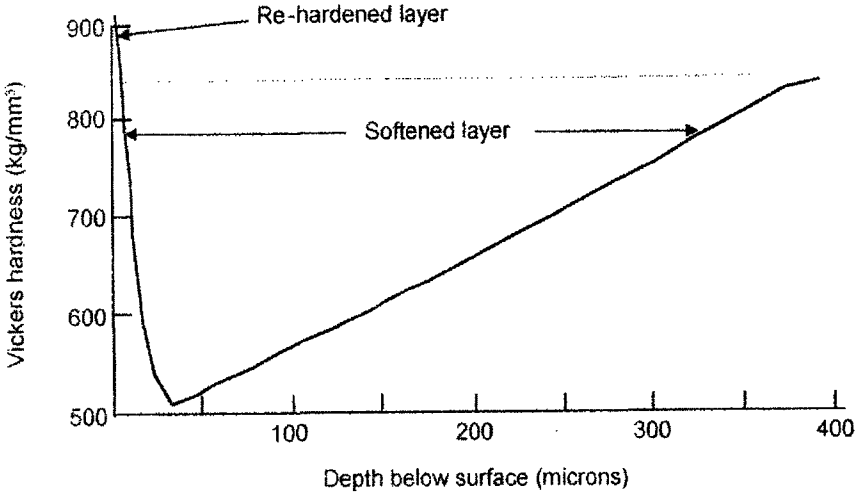

Figure 1.4 Microhardness variation below the workpiece surface caused by abusive grinding leading to re-hardening burn [18].

1.2 Scope of Thesis

Grind-hardening is a process that is still in its early stages of development. References [2-7] are the exclusive sources of information available in the public domain. Significant research on this process is essential in order to render the technology mature enough for industrial adoption. In this light, the objective of this research is to further the science and technology of this process, with a view to establishing a scientific framework for optimizing the process response. The research conducted in the present work comprised the following components:

1. Grinding experiments to ascertain the phenomenon of grind-hardening.

2. Formulation and calibration of a numerical thermal model to compute the temperature distribution beneath the ground surface to predict the incidence of surface hardening and the case depth.

3. Establishing experimentally validated process maps that identify grinding parameter combinations that result in grind-hardening.

1.3 Relevance to Industry

Niagara Machine Products (NMP), a division of Court Group of companies, is the industrial partner in this project. NMP specializes in the manufacture of automotive automatic transmission valves. Machining and grinding operations of these valves are accomplished in-house, whereas heat treating is sub-contracted to manufacture transmission valves made of free cutting steels. It is highly advantageous to adopt the grind-hardening process for integration into the production line. This would translate into a substantial business advantage in terms of reduced cost, lead time to manufacture and better control of component quality as the heat treatment process need no longer be outsourced. Furthermore, the technology represents an environmentally benign "green" process by way of having displaced an energy intensive heat treatment process.

1.4 Organization of Thesis

This thesis includes five chapters. A detailed literature review of previous investigations on temperature measurement and thermal modeling is discussed in Chapter 2 with particular emphasis on grinding heat and its effect on surface and subsurface microstructure of the workpiece. Chapter 3 details experimental equipment, methodology, and procedures used, including information on grinding conditions. Chapter 4 details numerical modeling of surface grinding process and presents a comparison with analytical results. This chapter also presents and discusses experimental results. Conclusions derived from the work and suggestions for future work comprise Chapter 5.

Chapter 2

Literature Review

This chapter is intended to provide an overview of research developments in grind hardening technology and heat transfer analysis during grinding. To predict the temperature distribution and the resulting alteration of surface layers, it is important to understand heat transfer in grinding. Analytical thermal models have been developed by many researchers for the calculation of generated temperatures and residual stresses. These thermal models have greatly clarified the importance of various physical processes involved in grinding, leading to the development of "Grind Hardening" technology.

2.1 Thermal Analysis of Grinding

There has been extensive research conducted in the thermal analysis of grinding. An overview of the major findings in this field follows.

One of the first analytical works on the thermal analysis of grinding was done by Outwater and Shaw [20]. They applied Jaeger's moving heat source theory [21] and Blok's [22] heat partition to obtain an equation for the temperature attained on the

ground surface at the tip of a grinding grit. Thus they considered the heat partition between the individual grains in the grinding wheel and the work material in the contact zone. They assumed the abrasive grains on an average to present a zero rake angle and considered the heat partition at the shear plane. They approximated this to the case of a plane slider of infinite width sliding on a perfect insulator as shown in Figure 2.1 and applied Blok's heat partition principle . They found the mean temperature across the shear plane to be 1163 °C (2125 °F). They reported that 65% of the shear energy passes off with the chip, while 35% flows into the workpiece. They also reported measured grinding temperature using the tool-work thermocouple technique and reported maximum temperature in excess of 1371 °C.

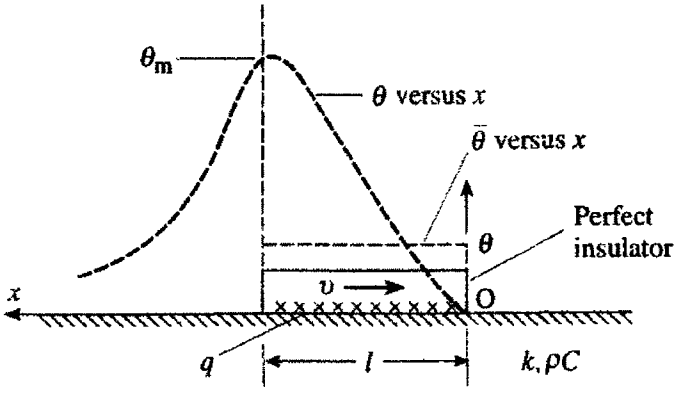

Figure 2.1 Two dimensional slider (perfect insulator) moving over a semi-infinite body [21].

Hahn [23, 24] reasoned from energy considerations that the principal heat generation is at the grain workpiece rubbing surface. This is because the shear plane energy assumption cannot account for the much larger energy experienced in practice. The heat generation is more accurately described by considering the energy to be dissipated at the contact between the workpiece and the grain, neglecting the shear plane energy.

Malkin and Anderson [25] recognized that the grinding heat is generated both

at the shear plane and along the wear flat of an abrasive particle as shown in Figure 2.2. They concluded that almost all of the plowing and sliding energies, and about 55% of the chip formation energy are conducted into the workpiece. So they calculated the overall fraction of griding energy entering into the workpiece as

$$\varepsilon = \frac{u_{pl} + u_{sl} + 0.55u_{ch}}{u} = \frac{u - 0.45u_{ch}}{u} \tag{2.1}$$

where u_{pl} is the specific plowing energy, u_{sl} is the specific sliding energy, u_{ch} is the specific chip forming energy and u is the specific grinding energy.

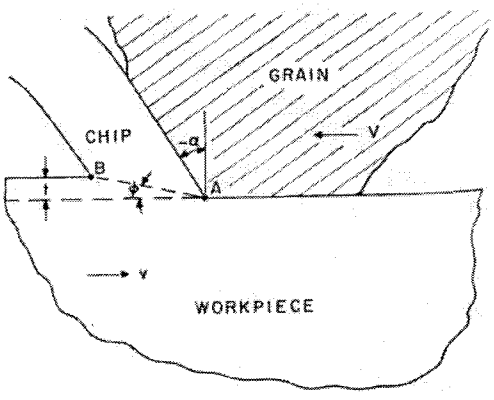

Figure 2.2 Locations of heat generation in grinding [25].

Ramanath and Shaw [26] studied the heat partition between an abrasive grain and the workpiece and obtained the thermal partition coefficient evaluated only from ratios of the thermal properties of the workpiece and the abrasive. Studies by Malkin [11] showed that most of the energy is consumed by sliding and rubbing. Therefore, as pointed out by Tonshoff et al. [27], rubbing and friction between the flank face of the grain and the workpiece are of particular importance in grinding. Therefore, it is appropriate to assume that the heat is generated at the interface between the abrasives and workpiece without distinguishing between the rake face, flank face or

the tip of the cutting point. On a global scale, the heat is generated at the interface between the wheel and workpiece.

Des Ruisseaux and Zerkle [28] extended Jaeger's solution by superposing a convective flux. They analyzed the heat convected from the workpiece by the grinding fluid. In this case, it is imagined that some of the heat conducted into the workpiece at a grain contact position is quickly conducted out of the workpiece again. If this happens quickly enough, the background temperature of the workpiece in the region where numerous grain contacts are taking place can be reduced. It was found that significant convective cooling would not occur in the contact region for conventional grinding at typical depths of cut.

Hahn [29] in a discussion of the paper [30] by Des Ruisseaux and Zerkle brought another important issue, namely the effect of various deflections that occur in grinding along the contact length, and consequently, the area of the contact zone. Other researchers followed this lead and investigated the effect of local deformation on the contact area in grinding [29, 31-34]. Rowe et al [35] reviewed the work conducted by many researchers and reported that the measured contact length can be 50-200% higher than the geometric contact length, and stressed that this effect should be considered when comparing experimental results with analytical results.

Rowe et al. [35, 36] developed an elegant analytical model to determine the grinding temperature by energy partition. They divided the workpiece temperature generated within the grinding zone into the following two parts, as illustrated in Figure 2.3.

1. Workpiece experiencing elevated background temperatures due to the distributed action of all the grains operating in the grinding zone. This analysis is designated as the wheel contact analysis or the global contact length.

2. Localized temperatures experienced at the abrasive grain tip-workpiece interface by spikes elevating above the background temperature. This is termed as workpiece spike temperature or the flash temperature. The analysis is designated as a grain contact analysis or local contact analysis.

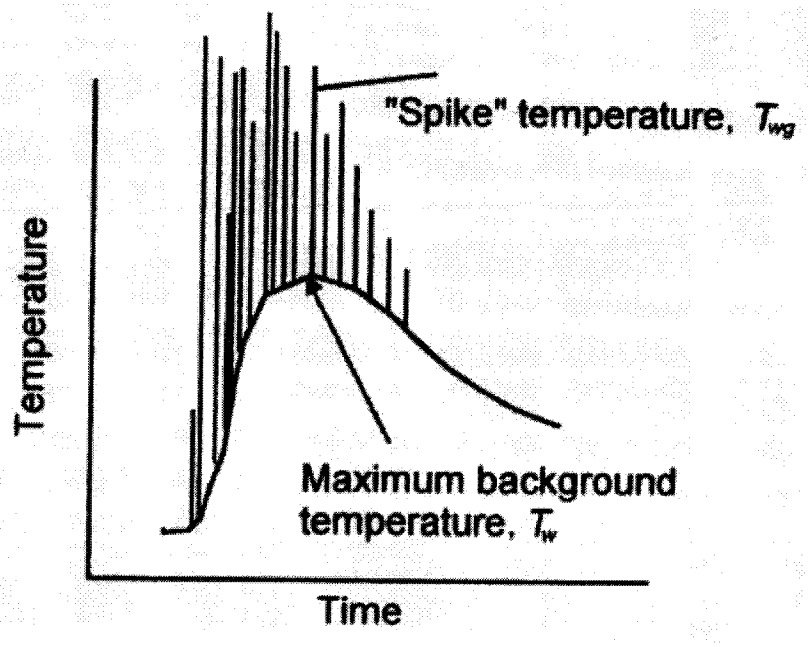

Figure 2.3 Illustration of temperature-time variation showing temperature spikes as well as background temperature [35].

For the wheel-work contact analysis, Rowe et al. [35, 36] considered the heat source at the workpiece as a band source moving across its surface at the workpiece speed. Similarly, the heat source at the wheel was likened to a band heat source moving across the wheel with the wheel speed. For the grain-workpiece contact analysis, the grain is modeled as a stationary body subjected to a constant circular heat source for the duration in the grinding zone. The grain temperature is determined from the Archard solution [37] for the stationary infinite body subjected to a circular heat flux. They conducted both grain contact analysis and wheel contact analysis and

compared the calculated temperatures with the experimental values. The workpiece surface temperature was measured using grindable thermocouples exposed at the workpiece surface. The thermocouple consisted of a chromel foil insulated on either side using mica. Using this technique, temperatures measured have demonstrated good agreement with predicted temperatures.

Rowe et al. [38] also modeled the energy partitioning to all four heat sinks analytically. The heat applied to the workpiece is likened to a band heat source moving across its surface at the workpiece speed. Similarly, the source applied to the wheel was likened to a band heat source moving across the wheel surface at the wheel speed. The heat flux into the workpiece is expressed as a product of the average workpiece background temperature and a heat transfer coefficient. Similarly, the heat flux into the grinding wheel is expressed as the product of the average grinding wheel contact zone temperature and another heat transfer coefficient.

Ju et al. [39] conducted the analysis of heat partition and temperatures in grinding including the effect of grinding fluid. At the local level he considered the interactions between the grains and the workpiece and at the global level between the wheel and the workpiece. At the global level, they also considered the workpiece as a 2D rigid body subjected to a steady moving heat source. They considered the global temperature as not the 'average' of the local scale events at a given time but also the 'cumulation' of the local events through all the previous times. On the local scale, since the contact area between the workpiece and grains is very small, the local moving heat source is treated as three-dimensional. In addition, since the contact between the workpiece and grains occurs only for a short time, the local moving heat source is not treated as steady but transient. For this case, the local temperature rise for the workpiece is calculated from Jaeger's solution for a rectangular heat source in motion for a finite time. Since the grain contact area is very small, they took the temperature

rise at the center as the average local temperature rise. Theoretically, all interacting grains contribute to the global temperature. They recognized that on the local scale, the action between the workpiece and grains might vary for different positions and for different grains. However, they took a typical condition of contacting grains as the average value. The geometry and heat distribution in plunge surface grinding are illustrated in Figure 2.4.

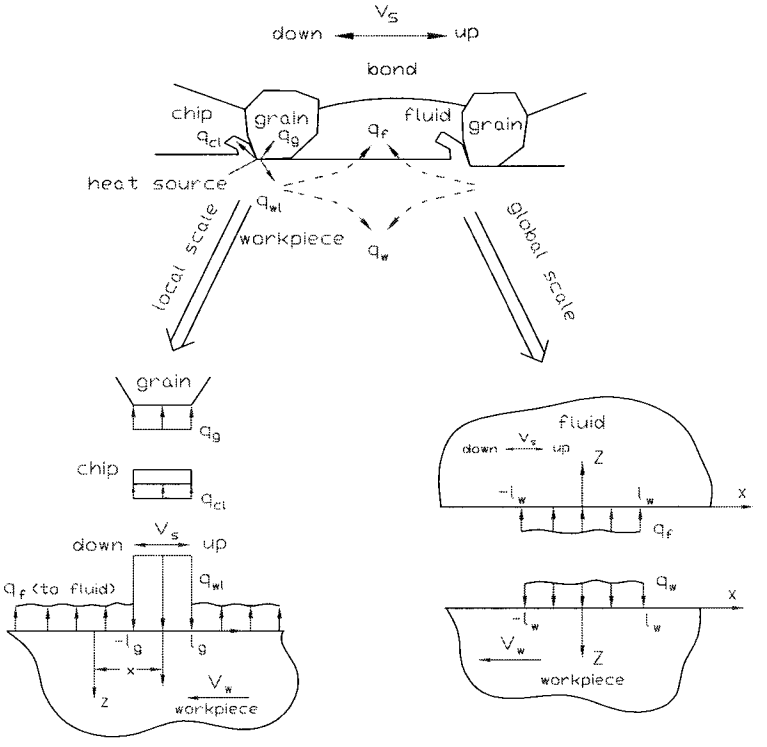

Figure 2.4 Illustration of geometry and heat distribution in plunge surface grinding [39].

Ju et al. also conducted experimental verification of grinding hardened steel with both aluminum oxide and cubic boron nitride (CBN) grinding wheels. They reported heat partition of 30% to wheel, 65% to work, and 5% to chips in up-grinding of steel with aluminum oxide wheel and 25% to wheel, 71% to work, and 4% to chips in down grinding. They found that heat partition varies over a wide range depending on

the grinding conditions. They also reported that on a local scale, the action between the workpiece and grains varies for different positions and different grains. Therefore the local grinding heat, and the heat partitioned locally to the workpiece vary with each grain and position. They showed that while the presence of grinding fluid can reduce the heat flux into the workpiece and workpiece temperatures significantly, it may not be effective inside the grinding zone in conventional grinding of steel with aluminum oxide grinding wheel due to fluid boiling.

Lavine [40] developed a simple theoretical model of convective heat transfer between the wheel and the workpiece surfaces and the grinding fluid. It was assumed that the grinding fluid completely fills the wheel pores and that the fluid and the wheel forms a composite solid, which moves past the workpiece at the wheel speed.

Lavine and Jen [41] developed separate models for heat transfer to the abrasive grain, the fluid, the workpiece using a conical grain model shown in Figure 2.5. They calculated heat transfer coefficients for each model using equations 2.2, 2.3 and 2.4 respectively.

$$h_g(x) = q''/\theta_g(z=0) = \sqrt{\pi(k\rho c_p)_g V_s/4xf(\zeta)} \tag{2.2}$$

$$h_f(x) = q''_f/\theta_f(z=0) = \sqrt{\pi(k\rho c_p)_f V_s/4x} \tag{2.3}$$

$$h_{wb}(x) = q''_{wb}/\theta_{wb}(z=0) = \sqrt{\pi(k\rho c_p)_w V_w/4x} \tag{2.4}$$

where function '$f(\zeta)$' is

$$f(\zeta) = \frac{2}{\pi^{1/2}1 - exp(\zeta^2)erfc(\zeta)} \tag{2.5}$$

q = Heat flux

θ = Temperature rise relative to ambient temperature

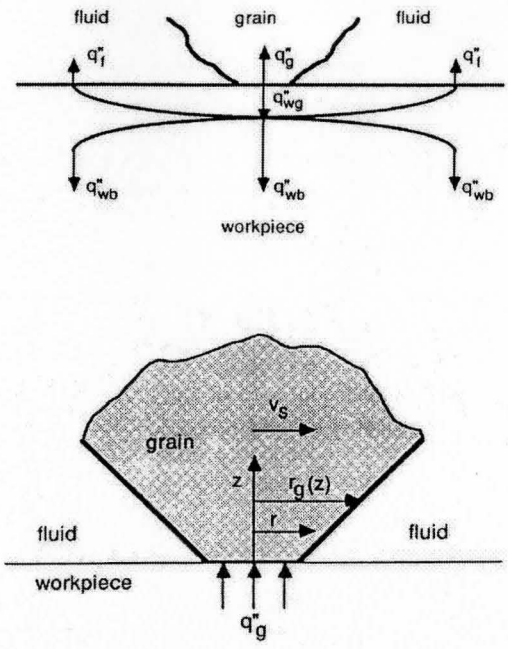

Figure 2.5 Conical grain model for heat transfer in an abrasive grain [41].

k = Thermal conductivity

ρ = Density

C_p = Specific Heat

V_s = Wheel velocity

x = Distance from the beginning of grinding zone

h = Heat transfer coefficient

$\zeta = (\pi \alpha_g x / A_o V_s)^{1/2}$

A_o = Individual grain-workpiece contact area

and subscripts g = Grain, f = Fluid and wb = workpiece background.

These models were then coupled to yield the temperature at the grinding interface between the workpiece and the wheel. Making use of heat transfer coefficients

defined in equations 2.2, 2.3 and 2.4, the coupled equations become:

$$\frac{q''_{wb}}{h_{wb}(x)} = \frac{q''_f}{h_f(x)} \tag{2.6}$$

$$\frac{q''_g}{h_g(x)} = \frac{q''_{wb}}{h_{wb}(x)} + \frac{q''_{wg}}{h_{wg}} \tag{2.7}$$

$$q''_{grind} = q''_{wb} + q''_g \tag{2.8}$$

$$q''_{wg}A_g = q''_{wb}A_{tot} + q''_f(A_{tot} - A_g) \tag{2.9}$$

where subscripts *grind* is grinding power, *wg* is workpiece under grain and *tot* is total. The coupling requires temperature match at the workpiece-fluid interface and the workpiece-grain interface. The model takes into account the elevated temperature underneath a grain which affects the fraction of the grinding energy that enters the grain and the workpiece. The work of Jen and Lavine was limited to large Peclet numbers and down grinding. Demetriou and Lavine [42] then extended the convective heat transfer model they developed previously to cover both up-grinding and down-grinding.

Kohli et al. [43] initially assumed a heat partition fraction for the work and used Jaeger's moving band heat source solution to calculate the temperatures at the interface on the work material side first. They measured the temperature using K-type chromel-alumel (30 gauge wire) thermocouple and compared the calculated results with the experimental. The obtained final heat partition by adjusting the initially assumed heat partition fraction for the work and repeating the calculations until the maximum temperature rise is matched with the experimental values. This way, they obtained the heat partition fraction to the work to be 60-75%, and to the wheel to be 25-40% for the case of grinding steel with an aluminum oxide grinding

wheel.

The maximum surface temperature on the workpiece side of the interface is calculated by considering the grinding zone as a band heat source moving along its surface at the workpiece speed. Maximum surface temperature on the wheel side is calculated similarly, by considering the same band heat source moving at the wheel speed. By matching the maximum surface temperatures on each side of the interface, an analytical expression for the fraction of the total energy conducted to the workpiece was obtained. This would result in a temperature distribution on the wheel side to be different from that on the workpiece side. But temperatures should match on both sides at each point along the grinding zone. For a given heat intensity distribution, the energy partition must satisfy the compatibility requirements, namely, the temperature on the wheel surface everywhere along the grinding zone.

Guo and Malkin [44] investigated the variation of the energy partition along the length of contact in grinding. They considered the abrasive grains and the grinding fluid filled in the pores of the wheel as a thermal composite moving through the grinding zone at the wheel speed. They modeled the energy partition to the workpiece by setting the temperature of the workpiece surface equal to that of the composite surface at every point along the grinding zone, which allowed for the energy partition along the grinding zone. They considered both rectangular and triangular distribution of heat flux and calculated the temperature using Jaeger's moving heat source theory. According to them, the theory predicts similar maximum temperature for constant energy partition but different temperature distributions. They developed a numerical algorithm, since a close form solution to the energy partition could not be obtained. They applied the analysis to obtain energy partition for several representative grinding cases. They reported that the energy partition to the workpiece is approximately constant along the grinding zone for conventional down-grinding but varies signifi-

cantly for up-grinding. This is because maximum temperature in up-grinding is close to the leading edge and the heated material at this location is subsequently removed as the workpiece passes under the wheel.

Obikawa et al. [45] conducted FEM simulations of fine grinding to determine the heat partition. They also measured the temperatures using a thermocouple consisting of a fine constantan wire (0.2 mm in diameter) welded to the bottom of a small hole drilled under the workpiece. Initially, they assumed a heat partition fraction for the work and computed the temperatures at the interface on the work side. By matching the computed and experimentally measured temperatures, they obtained a heat partition fraction of approx. 80% to the workpiece. They found the diameter of the thermocouple hole in the workpiece to have a significant influence on the heat partition fractions. They estimated the heat partition to the work without the hole to be approx. 50% by measuring the temperature using thermocouples of different diameters and extrapolating to zero diameter.

Malkin [46] calculated the local temperature distribution at an abrasive grain as the sum of two moving heat sources, one associated with the chip formation energy, which is distributed over the shear plane, and the other due to sliding between the wear flat and the workpiece. He calculated the maximum grinding zone temperature (T_{max}) using equation 2.10. The grinding energy was assumed to be uniformly distributed over the apparent area of contact between the wheel and the workpiece. He reported peak temperatures at the abrasive grain cutting edge close to the melting point of the workpiece.

$$T_{max} = \frac{1.13\alpha^{1/2}a^{3/4}V_w^{1/2}(u - 0.45u_{ch})}{kd_e^{1/4}} \tag{2.10}$$

where

α = Thermal diffusivity

a = Wheel depth of cut

V_w =Table speed

u = Grinding specific energy

u_{ch} = Specific chip formation energy

D_s = Wheel diameter

k = Thermal conductivity

Hou [47] considered the grain-workpiece interactions at the local level and the wheel-workpiece interactions at the global level. The workpiece temperature in the grinding zone was taken as the sum of the background temperatures due to distributed action of all the grains operating in the grinding zone (global thermal analysis) and the localized temperature spikes experienced at the abrasive grain tip-workpiece interface (local thermal analysis). They took into account the stochastic nature of distribution of abrasive grains to determine the grinding temperatures and heat partition. They estimated that the percentage of actual contacting grains is only 3-4% and the actual cutting grains are only 0.14-0.17%. The heat partition in grinding with conventional abrasives was found to be 17% into the chip, 70-76% into the work, and 6-13% into the abrasive.

Thermal models described above can be categorized and summarized in at least three type of thermal models.

1. First type of models consider only the grain-work interactions to determine the grinding temperatures as well as the heat partition. These analyses use Jaeger's heat source solution [21] and Blok's heat partition solution [22]. These models provide results significantly different from experiments.

2. The second approach considered the interface contact zone between the wheel and workpiece as the heat source. This method also gave somewhat unrealistic heat partition as it considers the heat source relative to the workpiece moving at the workpiece velocity and relative to the wheel at the wheel velocity. As a result, much of the heat goes into the grinding wheel than into the work material while it is just the opposite in practice.

3. The third method is a combination of the above two methods, which represents the heat transfer process more accurately. It uses the grain-workpiece interactions at the local level and wheel-workpiece interactions at the global level. The actual temperature is obtained by combining the two. This method gives more accurate values of heat partition as well as the grinding temperatures.

In the context of the heat transfer in grinding presented thus far, the next section details an overview of the grind hardening process.

2.2 Grind Hardening

One of the first experimental works on grind hardening was by Brinksmeier and Brockhoff [2]. They introduce this new surface treatment process that makes use of the heat generated in grinding. They carried out fundamental investigations to establish how the thermo-mechanical influence of a grinding process can be utilized for controlled surface hardening of components. For the attainment of grind hardening, they used standard alumina grinding wheels and rough grinding conditions. They observed a heat-treated zone (HTZ) to a depth of 300 μm beneath the surface with a significant increase in hardness. Typical case depth hardness profile and metallographic cross section of the ground surface obtained in their experiment is

shown in Figure 2.6.

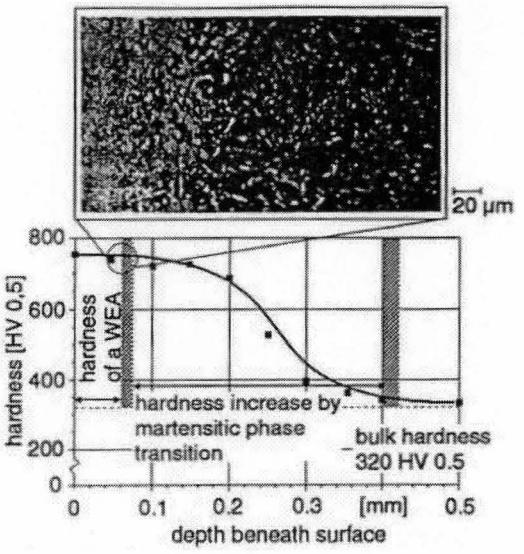

Figure 2.6 Heat treatable steel (AISI 4140) hardened by grinding [2].

They observed two distinct regions in the HTZ. Thick white etching area (WEA) of a few μm thickness at the surface with an extremely high hardness, followed by a hardened structure consisting of martensite and carbides. They concluded that an effective range up to 1 mm appears realistic in grind hardening with proper selection of workpiece material, wheel depth of cut and table speed.

Brockhoff [3] did further comprehensive experimental investigations on this concept. He discussed the influence of various process parameters on grind hardening and pointed out that the depth of cut, feed speed and wheel type are the most important process parameters for grind hardening. He measured specific cutting power P_c'' as well as specific energy e_c'' using equations 2.11 and 2.12 to assess hardening results.

$$P_c'' = \frac{F_t.V_s}{a_p.l_g} \tag{2.11}$$

$$e_c'' = R.P_c''.t_c \tag{2.12}$$

where F_t is tangential force, V_s is cutting speed, l_g is the contact length and a_p is acting wheel width. R is partition ratio and t_c is contact time.

In terms of the effect of depth of cut on case depth, he concluded that increasing it led to higher energy entering the workpiece, and consequently, higher hardness depths can be achieved. The effect of depth of cut on the case depth is shown in Figure 2.7.

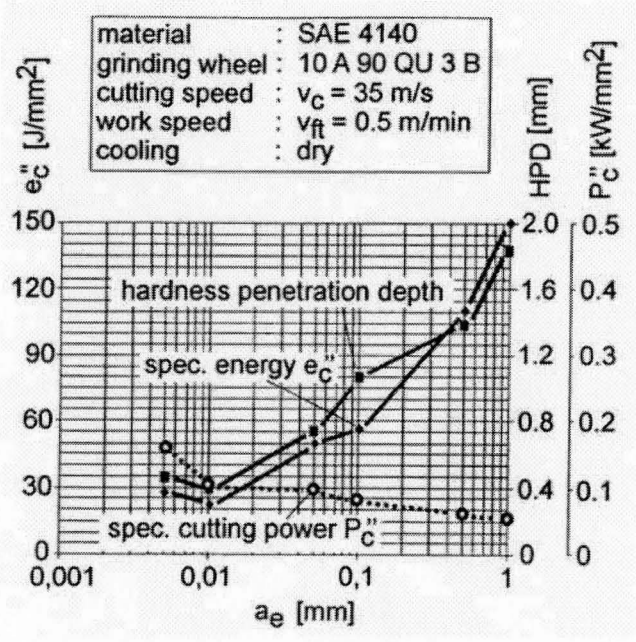

Figure 2.7 Hardening results depending on depth of cut [3].

As for the work speed, increasing or decreasing it would alter the contact time between grinding wheel (heat source) and a fixed point on the workpiece surface and the quantity of heat penetrating into the workpiece. He inferred two main effects of feed speed. Firstly, at very low feed speed, the specific traveling energy e_c'' is high due to the low cutting power and hence the extent of the hardened layer is reduced. Sec-

ondly, at a very high speed, the cutting power P_c'' increases, but due to the decreased contact time and lower specific traveling energy e_c'', the extent of the hardened layer is reduced again. It was therefore concluded that an optimal feed speed achieves the maximum case depth. The effect of feed speed on case depth is shown in Figure 2.8.

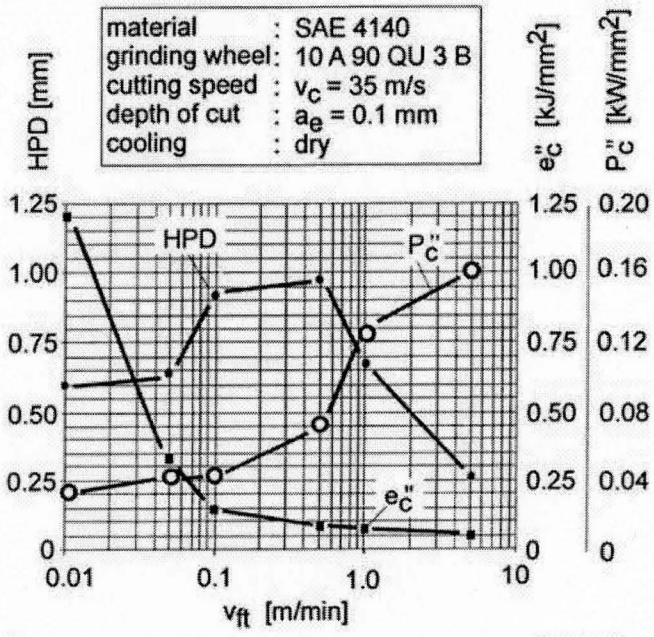

Figure 2.8 Hardening results depending on work speed [3].

Brockhoff in his paper [3] also compared vitrified and resin bonded wheels. He concluded that resin bonded wheels are better for grind hardening because resin bonded wheel flexes which results in more contact area, ultimately generating higher heat flux.

Venkatachalapathy et al. [5] studied grind hardening in cylindrical grinding configuration. They carried out this experimental study in grinding AISI 6150 and AISI 52100 steels with an aluminum oxide grinding wheel. They developed a theoretical model to predict the partition ratio and workpiece temperatures using the grain contact zone model due to Rowe et al. [48]. Proportion of heat entering into the

workpiece to the total heat produced was calculated using Equation 2.13.

$$1/R^{'} = 1 + V_s/V_w.[(k\rho c)_s/(k\rho c)_w]^{1/2} \tag{2.13}$$

where $\sqrt{(k\rho c)_s}$ is wheel bulk thermal coefficient, $\sqrt{(k\rho c)_w}$ is workpiece bulk thermal coefficient, V_s is cutting speed and V_w is speed of workpiece. Equation 2.13 calculates heat partitions without considering the energy convected away by the chips and coolant. Allowing the energy convected away by chips (e_{cc}) and coolant (e_{cf}), the predicted partition ratio is reduced, i.e.,

$$R = R^{'}[1 - (e_{cc} + e_{cf})/e_c] \tag{2.14}$$

Where e_c is specific chip energy (J/mm^3). They used typical values of $e_{cc} = 6$ J/mm^3 and $e_{cf} = 0$ due to Howes et at [49] and found partition ration of 0.73 and 0.74 for AISI 52100 and AISI 6150 respectively. From the calculated value of heat partition, the heat flux entering into the workpiece is calculated using following equation:

$$R = Q_w/Q_t = 0.83b\sqrt{(k\rho c)_w}.\sqrt{V_w}.\sqrt{l_g.\theta_m/Q_t} \tag{2.15}$$

where Q_w is the amount of heat entering into the workpiece, Q_t is total heat produced, l_g is the grinding contact length and θ_m is the initial workpiece temperature.

They then carried out experimental investigations with varying depths of cut, feed and number of passes. For depth of cut and feed speed, they had the similar results as of Brockhoff [3]. For number of passes, they inferred that there is an increase in hardness up to 14 passes but then it starts to decrease as shown in Figure 2.9 which may be attributed to the retempering of the hardened surface. They also examined the ground surface for the micro cracks using electromagnetic crack detector. No

surface crack was found in the grind hardened components and surface finish was in the acceptable range of 0.1 to 0.16 μm R_a.

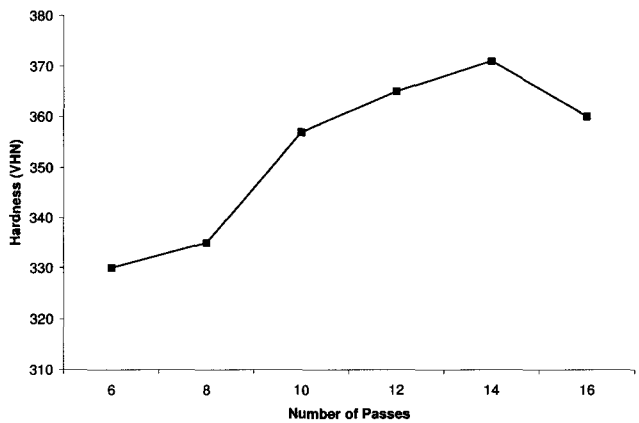

Figure 2.9 Influence of number of passes in grind hardening [5].

In contrast to previous work on grind hardening done using conventional abrasive aluminum oxide, Fricker [4] used cubic boron nitride (CBN) wheel for his experimental work on grind hardening. One of the major differences between CBN and aluminum oxide is the thermal conductivity of the two abrasives [50, 51]. While aluminum oxide acts as an insulator, CBN abrasive is able to remove a significant proportion of heat from the grinding zone by heat transfer through abrasive segments into the steel hub of the wheel. Heat partition ratios for aluminum oxide is typically around 0.8 [50, 51, 52], where as for CBN wheel it is around 0.4 [50, 51, 53].

Fricker developed a thermal model for dry cylindrical grinding of 42CrMo4 crankshaft steel using cubic boron nitride (CBN) wheel to predict subsurface time-temperature profile. He used Jaeger's [21] two dimensional thermal model of a moving heat source on the surface of a half space to predict workpiece temperatures. He then carried out experimental investigations to study the effect of two main process variables: depth of cut a up to 1 mm and work speed V_w up to 25 mm/s. The maximum case depth was found to be 1.7 mm for a wheel depth of cut of 0.5 mm and table

feed of 500 mm/min. Residual stresses were found to be compressive and the ground surface was free of micro-cracks.

From experimental hardness results, Fricker plotted specific energy against material removal rate. Experimental points were separated into those where grind hardening was measured and those where there was no grind hardening. The polynomial fit applied to the proportion of specific energy entering the workpiece as heat, as a function of specific removal rate, and is shown in Figure 2.10. There is a distinctly reducing trend of the specific energy as specific material removal rate is increased to achieve grind hardening. He then produced a theoretical chart shown in Figure 2.11 for grind hardening over a range of work speeds and depths of cut. The solid curves show the onset of grind hardening at a particular depth 'ζ' beneath the final ground surface. The dashed curve shows the upper limit imposed by melting of the workpiece surface. He then took one particular grind-hardening depth, namely ζ=0.5 mm, from Figure 2.11 and used in Figure 2.12. Experiment points where grind hardening was achieved over ζ=0.5 mm were plotted in Figure 2.12. The agreement between the experimental results and theoretical prediction was considered to be good.

Nguyen [7] used liquid nitrogen as a coolant for his grind hardening experiments to avoid problems like poor surface finish and precision, tensile residual stresses, damaged microstructure and severe oxidation. He used AISI 1045 steel for his experiments and compared microhardness, microstructure and residual stresses using coolant (Noritake SA-02, flow rate = 18.8 l/min.), dry air (ambient temperature = 20 °C) and liquid nitrogen (flow rate = 2.18 l/min.). Experiments were performed on a surface grinder and grinding conditions were kept constant (wheel speed = 23 m/sec, table speed = 400 mm/min. and wheel depth of cut = 20 μm). He found that the micro-hardness (HV) of the subsurface remained unchanged ($HV_{(500g)}$=200) after grinding with coolant. However, the micro-hardness due to the grinding in dry

air increased to $HV_{(500g)}$=750 which is 3.75 times higher than that of original steel and micro-hardness due to grinding in with the liquid nitrogen was even higher, $HV_{(500g)}$=1100 which is 1.46 times higher than that of the hardness developed by the grinding in dry air. The effect of liquid nitrogen on the surface hardness is shown in Figure 2.13.

Nguyen compared residual stresses in subsurface of ground components produced with different cooling media. He observed compressive residual stress for both grinding with Noritake coolant and liquid nitrogen. On the contrary, grinding in dry air was observed to have tensile stresses along the whole depth of hardened layer. A comparison of the microstructure of martensite obtained from liquid nitrogen and dry air was also made. He inferred that martensite from liquid nitrogen is composed of fine and nearly circular grains with a characteristic dimension of 0.2 - 0.3 μm where as martensite laths from dry air are grouped in packets with lengths of 2 - 3 μm.

Zarudi [54] also studied grind hardening of AISI 4140 steel using compressed air

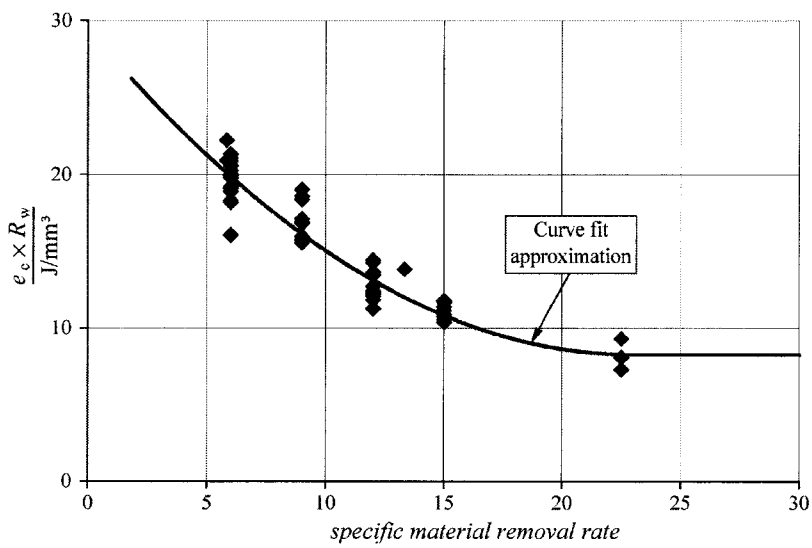

Figure 2.10 Specific energy verses material removal rate for CBN wheel experiments [4].

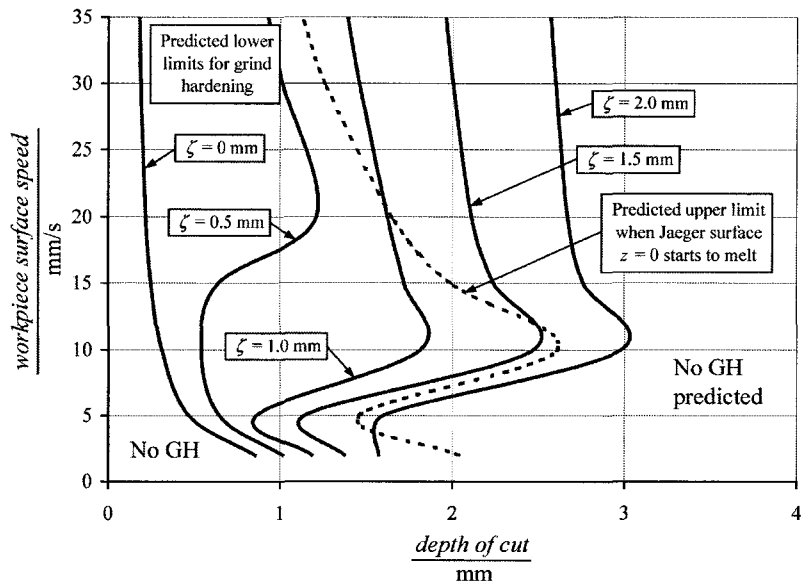

Figure 2.11 Prediction of occurrence of grind hardening to a particular depth of cut [4].

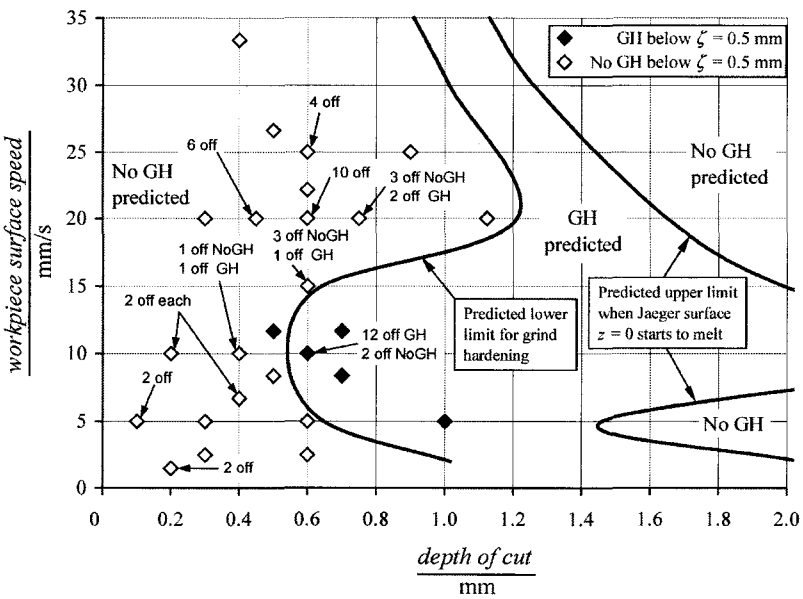

Figure 2.12 Comparison of the predicted and experimental occurrence of grinding hardening [4].

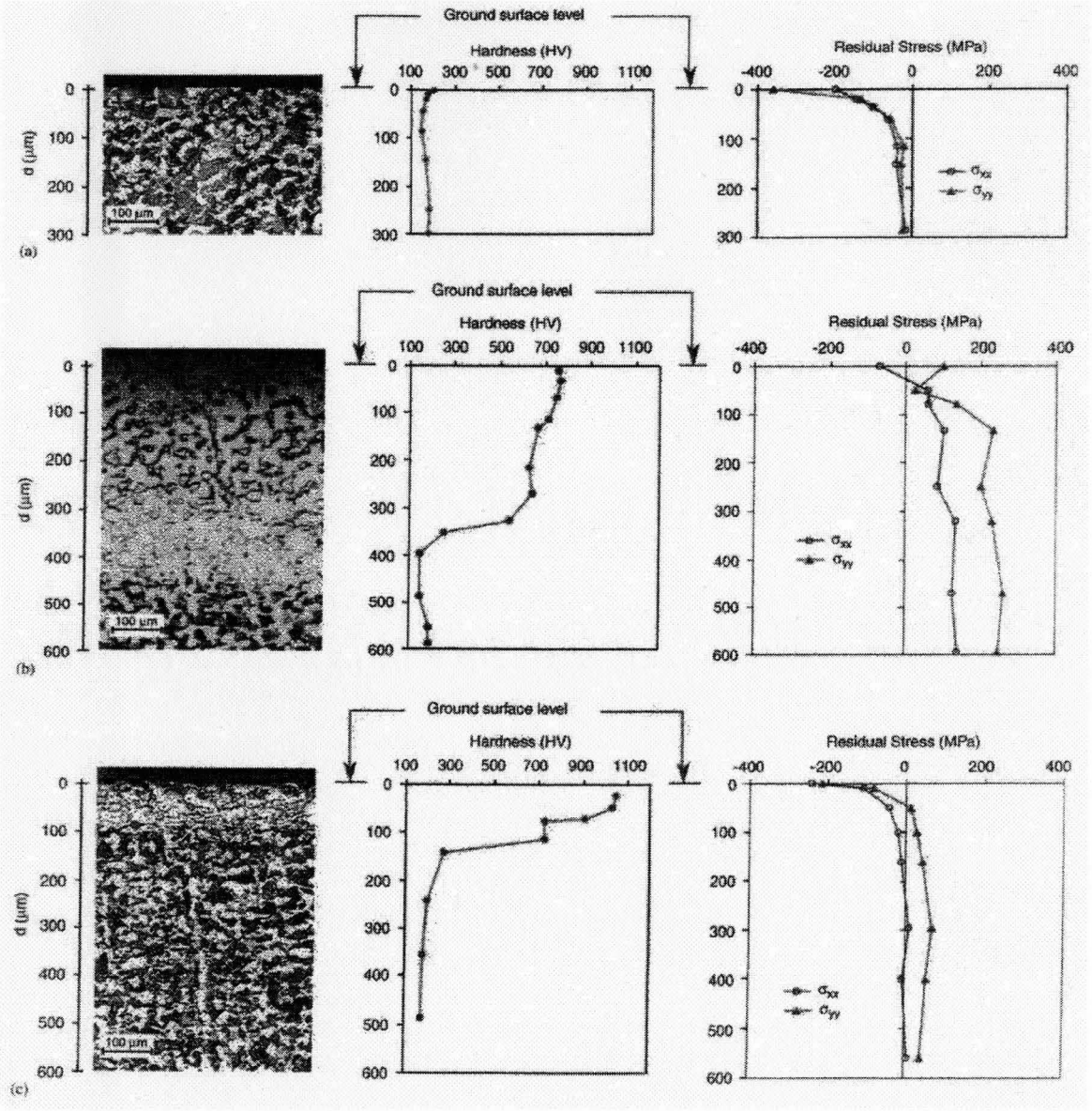

Figure 2.13 Subsurface structure, hardness and residual stresses after griding (a) with coolant; (b) in the dry air; (c) with liquid nitrogen [7].

as a coolant. The main focus of his research was microstructural analysis of subsurface after grind hardening. He compared Grinding Induced Layer (GIL) obtained through grind hardening to ordinary martensite (OM) obtained from heating the specimen to 850 °C and quenching vigorously in oil. Comparison for wear and fatigue resistance

of these two samples was made, the results of which are shown in Figures 2.14 and 2.15.

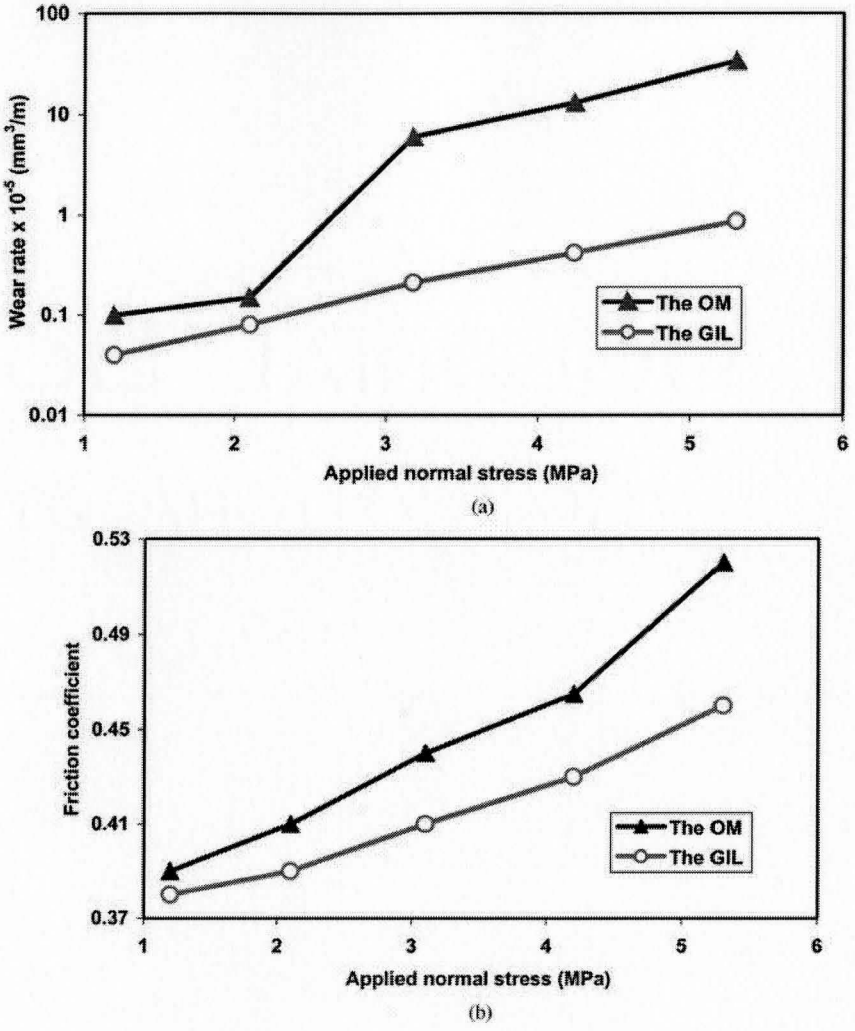

Figure 2.14 Wear and friction properties of ordinary martensite and grinding induced layer [54].

Zarudi concluded that wear resistance and fatigue life of GIL is superior compared with the OM. He argued that the superior property of high wear resistance and low friction coefficient of the GIL is due to its special microstructure. Both, grain

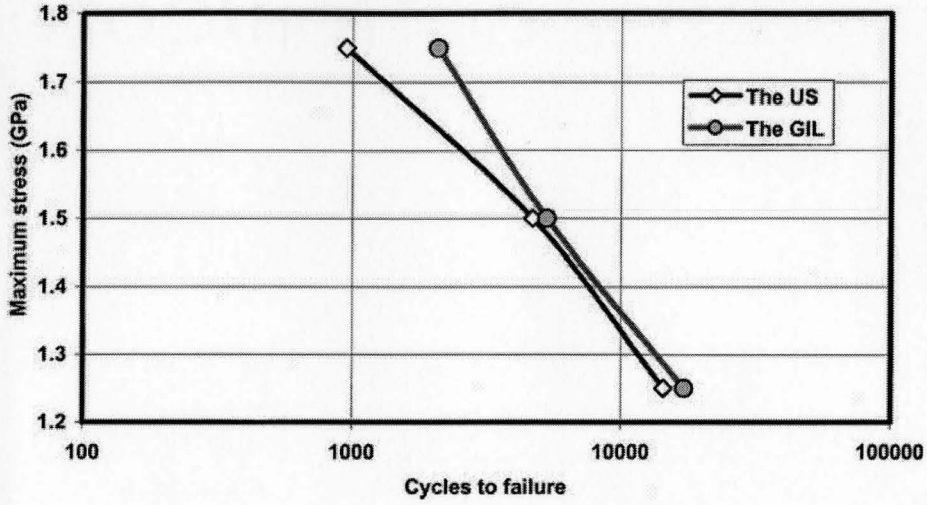

Figure 2.15 Fatigue life of ordinary martensite and grinding induced layer [54].

refinement and polygonal dislocation arrangement enhance the thermal and mechanical stability of the structure. Since the energy consumption for changing the GIL structure is higher, the GIL possesses a better wear resistance. He also found high compressive residual stresses in GIL, which play an important role in the improvement of the fatigue life of a component.

2.3 Summary

Results reported in the papers pertaining to 'thermal modeling of grinding' indicate that the temperatures and partition ratios are dependent on specific energy of the grinding process and on the thermal properties of the workpiece and the abrasive. Temperatures have been reported to exceed the upper critical temperature line with the partition ratio of heat flux into the workpiece ranging from 0.70-0.75 with conventional abrasives. Moreover, the distribution of heat flux has been considered to be uniform as well as triangular. Maximum temperatures are reported to occur at the trailing edge for a uniform distribution and at the mid point of the band for a

triangular distribution.

The information reviewed provided important insight into the present research on grind hardening technology. In the context of the work reviewed, numerical analysis was performed with assumption of uniform heat flux distribution in the grinding zone with a partition ratio of 0.7. Experimental work was performed to validate and quantify the grind hardening process to achieve required surface hardness and case depth. The above aspects of this research are presented in chapter 4. The next chapter provides information on the experimental work.

Chapter 3

Experimental Details

The purpose of the experimental phase of the investigation was to validate the grinding conditions and grinding power data obtained from numerical analysis detailed in chapter 4, in terms of realizing an effective grind hardening process. Grinding experiments were conducted both on AISI 52100 and AISI 1045 steels.

3.1 Grinding Setup

3.1.1 Machine Tool

Grinding experiments were performed on a horizontal spindle surface grinder (Blohm Planomat 408) shown in Figure 3.1. This machine tool had a maximum spindle speed of 8500 rpm, spindle power of 18.5 kW and a table feed rate of 30 m/min.

A Hall Effect transducer was installed on the machine to measure the grinding spindle power. Using Hall Effect devices instead of the traditional current transformers (CT) and voltage transformers (PT) greatly simplified installation. Accuracy is

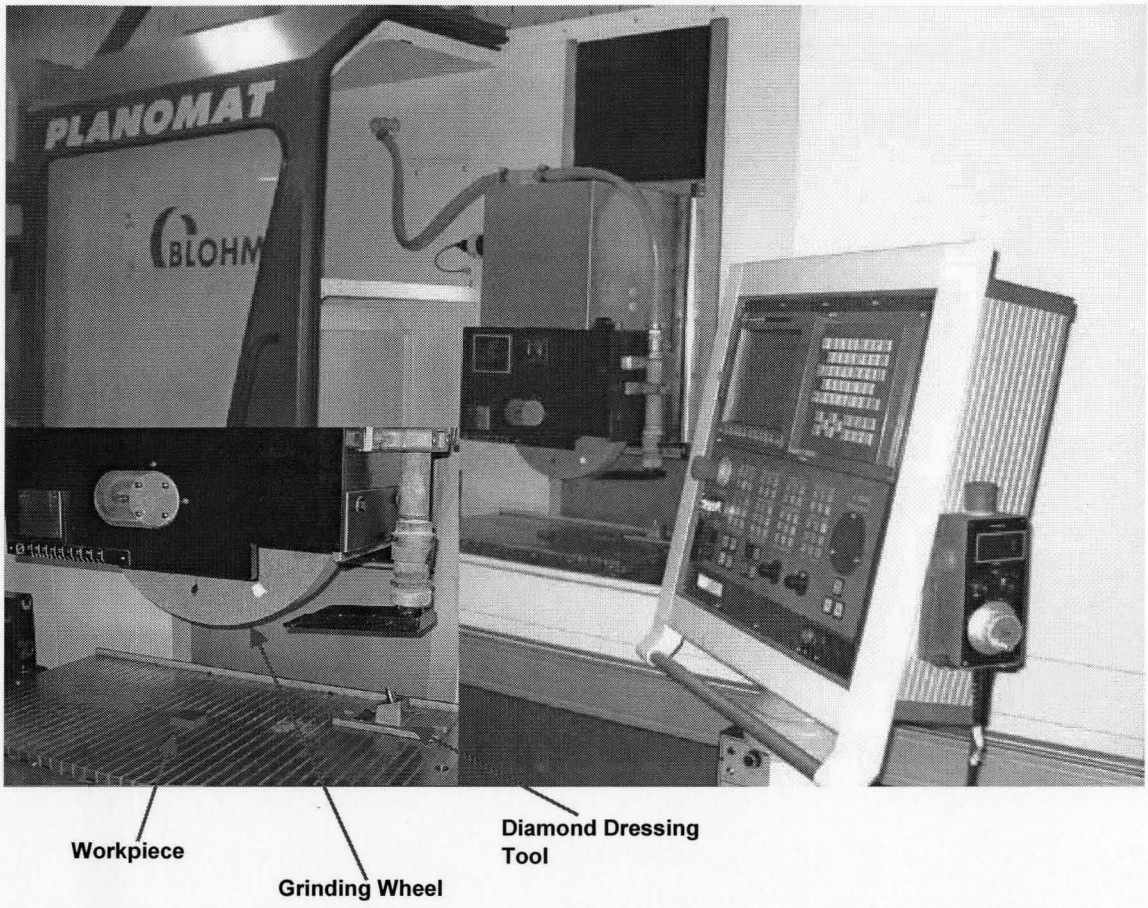

Figure 3.1 Blohm Planomat 408 CNC surface grinding machine.

greatly improved by eliminating the phase shift errors from CTs and PTs which can be large at low power factors. The Hall Effect sensors are sensitive to low and high frequencies, works on the output of variable frequency drives, has fast response, provide linear output and are immune to magnetic interferences. Hall Effect transducer used in this work was UPC-KWH the technical specifications of which are listed in Figure 3.2.

Figure 3.3 shows a sketch of the Hall Effect sensors mounted on the machine tool. Each phase of the grinding spindle motor is passed through three balanced Hall Effect Sensors, each with a flux concentrator. A voltage sample from each phase is pro-

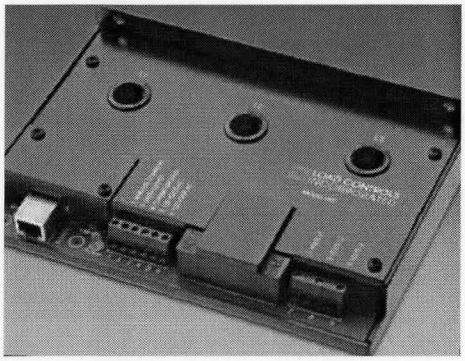

Hall Effect Transducer Specifications	
Accuracy	0.5% of FSR
Full Scale Capacity	5HP to 150 HP
Analog Output - Current	4 - 20 Milliamp
Analog Output - Voltage	0 - 10 Volts DC
Response Adjustment	0.5 sec. to 12 sec.
Frequency	3Hz to 1kHz
Power Comsumption	6VA at 120 Volts

Figure 3.2 Technical specifications of UPC-KWH Hall Effect transducer.

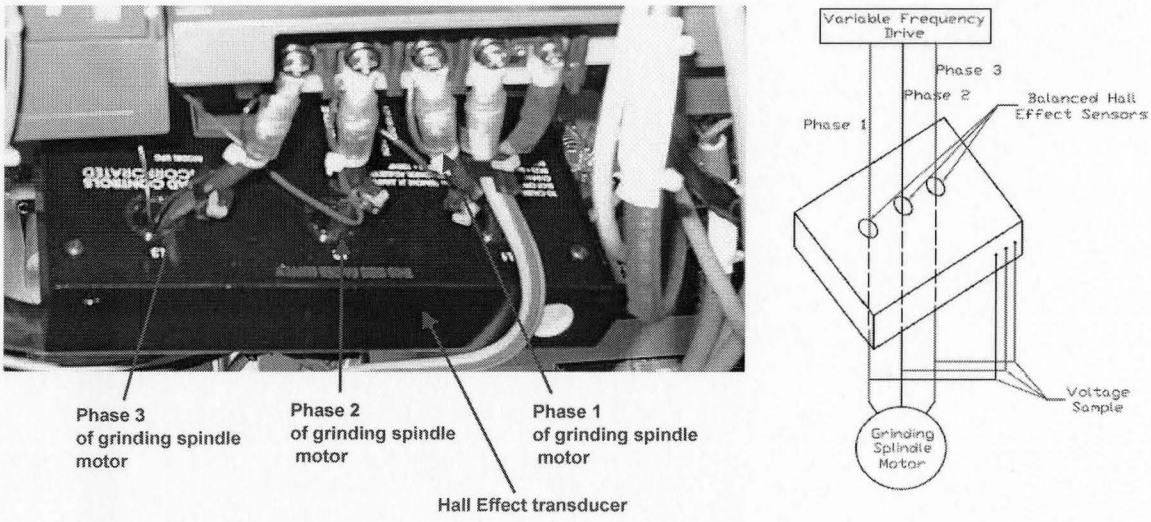

Figure 3.3 Instrumentation for measuring grinding power and sketch of its installation.

vided to the sensor. The Hall Effect semiconductor then does a vector multiplication of the current flow and voltage. The output is proportional to power.

The Hall Effect transducers were connected to a computer through a Data Acquisition System (DI-158U). Technical specifications of DI-158U are listed in the Figure 3.4. The spindle power was recorded using WinDaq software as a digital output in kW using this data acquisition system. A typical plot of spindle power versus time is shown in Figure 3.5.

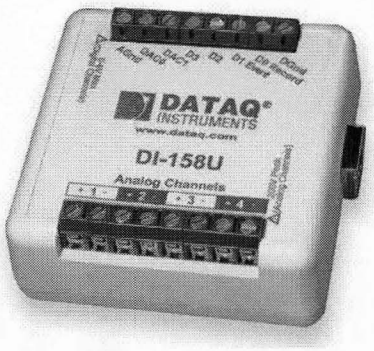

Data Acquisition system (DI-158) Specifications	
Accuracy	0.1% of FSR
No. of Channels (Analog Input)	4
Channel configuration	Fixed differential
Resolution	12 bit
Gain Range	±10 Volts
Max. sample rate	14,400 Hz

Figure 3.4 Technical specifications of DI-158 data acquisition system.

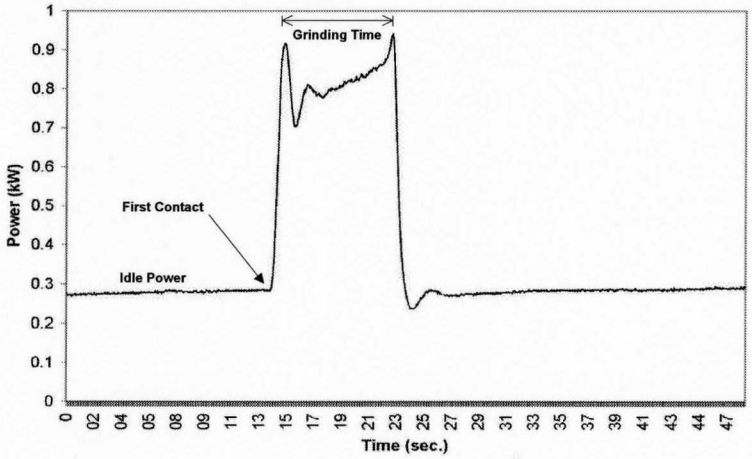

Figure 3.5 A typical grinding spindle power plot obtained using the Hall Effect transducer.

The plot shows power consumption during single pass of a plunge surface

grinding process. Initially machine tool is consuming power of about 0.28 kW. This is the amount of power required to idle the wheel. There is an increase in power (0.9 kW) when the wheel engages the workpiece. After completion of a single pass it drops back to the idle power value. The idle power is subtracted from the total power to determine the power corresponding to the grinding operation.

3.1.2 Grinding Wheel

The grinding wheel specification decisively influences the heat dissipation in grinding process. In order to maximize the heat flow into the workpiece, corundum wheels are preferred due to their lower heat conductivity compared to CBN wheels [50, 51]. To maximize heat generation and conduction into the workpiece, aluminum oxide grinding wheels (Norton 64A60-K9V127) were used in this work. The poor thermal conductivity (33.5 $Wm^{-1}K^{-1}$) of alumina causes most of the generated heat to dissipate into the workpiece. The wheels used were vitrified bonded. Vitreous bonds are essentially glasses made from the high temperature sintering of powdered glass frits, clays and chemical fluxes such as feldspar and borax. Vitrified bond was considered because of its high temperature stability and rigidity, and the ease of truing and dressing. The wheel specification is given in Table 3.1.

Table 3.1 Aluminum Oxide grinding wheel specification

Wheel Type	64A60-K9V127
Wheel Diameter	304.8 mm
Wheel Width	38.1 mm
Bond Type	Vitrified

3.1.3 Workpiece

Considering hardenability and application, AISI 1045 and AISI 52100 materials were selected for this study. AISI 52100 steel is used extensively in the manufacture of ball and roller bearings and crushing machinery, and AISI 1045 steel was chosen because such steels are typical candidate materials for a variety of automobile components that require local hardening. Both of these steels are characterized by good hardenability. Chemical composition and thermo-mechanical properties of these materials are give in Tables 3.2 and 3.3 respectively.

Table 3.2 Chemical compositions of AISI 52100 and AISI 1045 (wt.%)

	52100	1045
Carbon	0.98-1.1	0.42-0.5
Manganese	0.35	0.6-0.9
Phosphorus	(Max) 0.025	(Max) 0.04
Sulphur	(Max) 0.025	(Max) 0.05
Chromium	1.45	-
Silicon	0.23	-
Iron	97	98.51-98.98

Table 3.3 Thermo-mechanical properties of AISI 52100 and AISI 1045

	52100	1045
Density, ρ (g/cm^3)	7.81	7.85
Young's Modulus, E (GPa)	210	205
Poisson's Ratio, ν	0.3	0.29
Thermal conductivity, K (W/m-K)	46.6	49.8
Specific Heat (J/g-°C)	0.475	0.519
Thermal Diffusivity, α (m^2/s)	1.25e^{-5}	1.30e^{-5}

Hardenability of steels is determined by the carbon content and alloying elements in a material [55]. Carbon content controls the hardness of the martensite. Increasing the carbon content increases the hardness of steels up to about 0.6 wt%. At higher carbon levels, the formation of martensite is depressed to lower temperatures and the transformation from austenite to martensite may be incomplete, leading to retained austenite (Figure 3.6). This composite microstructure of martensite and austenite gives a lower hardness to the steel, although the microhardness of the martensite phase itself is still high.

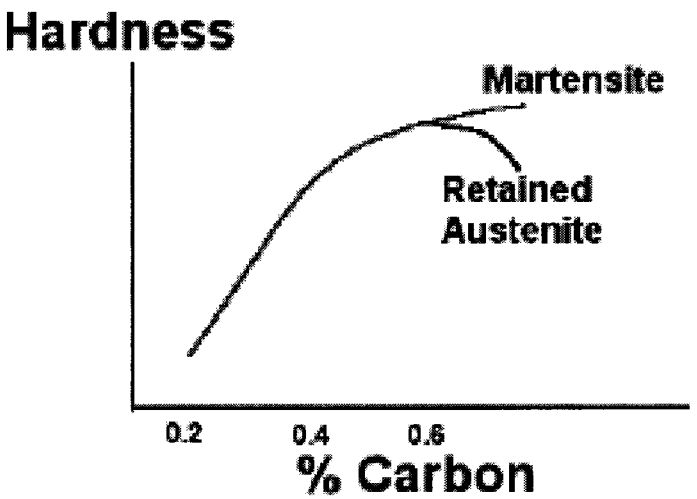

Figure 3.6 Effect of carbon content (wt%) on hardness [55].

The alloying elements Cr, Mo, Mn, Si, Ni and V all retard the phase transformation from austenite to ferrite and pearlite, decreasing the critical cooling rate significantly to form martensite [55]. The magnitude of the effect of alloying elements on hardenability is best described in terms of a carbon equivalent. A commonly used formula for calculating the carbon equivalent is:

$$E_c = \%C + (\frac{\%Mn + \%Si}{6}) + (\frac{\%Cr + \%Mo + \%V}{5}) + (\frac{\%Cu + \%Ni}{15}) \qquad (3.1)$$

Rectangular specimens for experiments were made from these materials with length = 30mm, width = 25mm and height = 12mm using a band saw. The top surface of the specimens were ground to plane the surface in order to eliminate variation of wheel depth of cut during experimentation.

3.1.4 Wheel Preparation

An out-of-balance grinding wheel will result in vibration with respect to the workpiece causing the wheel depth of cut to vary as the wheel rotates against the workpiece surface. An automatic wheel balancer (MPM BMT100) was hence used to balance the wheel on the grinder after mounting the wheel. Wheel balance was checked periodically during grinding at a wheel surface speed of 25 m/s, which is the speed used in all grinding experiments.

Wheel truing and dressing have a profound effect on the grinding performance [11]. Truing corrects the geometry of the wheel making it concentric with the spindle axis and ensures that the rim contacts the workpiece in its entirety during each wheel revolution. Dressing refers to conditioning of the rim surface topography to ensure that cutting edges are adequately protruding from the bond and thus are able to effectively penetrate into the workpiece material [56]. Figure 3.7a presents a schematic of the wheel surface after truing and dressing.

Truing and dressing are usually performed with the same dressing tool for conventional grinding wheels. In the grinding experiments conducted, a single point diamond dressing tool (PGW-CP1-75) was used to true and dress the wheel. The diamond point of dressing tool was set at a 15 degree drag angle pointing in the direction of wheel rotation (Figure 3.7b). The effectiveness and quality of conditioning process performed on a vitrified grinding wheel depends on the dressing lead f_d and

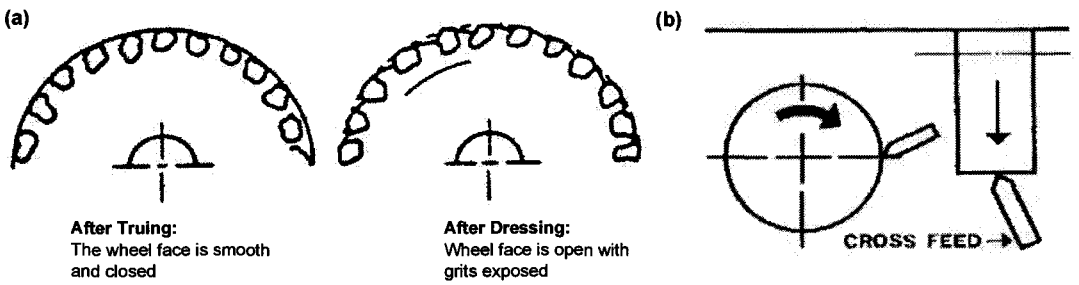

Figure 3.7 (a) Wheel profile and surface after truing and dressing (b) Diamond tool position during dressing and truing.

the dressing depth a_d [18]. The dressing tool moves across the wheel surface with a dressing lead f_d per wheel revolution while removing a dressing depth a_d and dressing width b_d as shown in Figure 3.8. The feed per revolution should always be sufficient to ensure several contacts between the dressing tool and the active grains of the wheel. An overlap ratio, U_d, can be defined as the result of dividing the contact width, b_d, of the dressing tool by the feed per wheel revolution, f_d:

$$U_d = \frac{b_d}{f_d} \tag{3.2}$$

The overlap ratio, U_d, should normally be greater than 2 and less than 10 to achieve satisfactory performance from a grinding wheel [18].

In this work, wheel was trued using single point dressing tool with truing parameters listed in Table 3.4. In order to establish dressing conditions that enabled grind hardening, experiments were conducted using coarse, medium and fine dressing conditions given in Table 3.5. A fine dressing operation refers to the combination of a small dressing lead and a small dressing depth. Conversely, the combination of a large dressing lead and a large dressing depth is described as a coarse dressing operation. The ultimate goal was to determine the optimum wheel topography where grind hardening could be achieved.

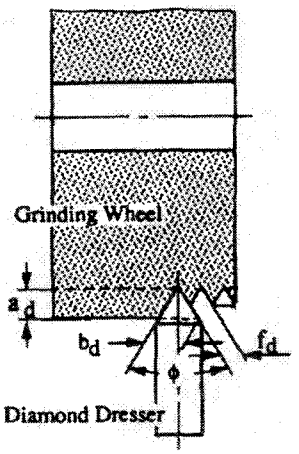

Figure 3.8 Kinematic dressing parameters [57].

Table 3.4 Parameters of wheel truing

Parameters	Value
Wheel Speed (m/s)	25
Dressing Depth (μm)	25.4
Transverse Feed Rate (m/min.)	0.5
Total Dressing Depth (mm)	0.25
Spark out passes	1

Table 3.5 Dressing conditions

Dressing Parameters	Fine	Medium	Coarse
Dressing Depth, a_d (mm)	0.005	0.015	0.025
Dressing Lead, f_d (mm/rev.)	0.05	0.15	0.25

3.1.5 Grinding Fluid

To attain the temperature above upper critical temperature line (Ac_3), dry grinding is preferred during grind hardening [3, 5-7]. No coolant was used during the experiments. After each experiment, the wheel was washed with the coolant to clear

swarf off the wheel.

3.2 Grinding Conditions

In this study, grinding parameters were chosen to evaluate the effect of depth of cut and feed speed on grind hardening of tempered and annealed steels. The parameters selected were based on the information available in the literature [2-7] and from FEA simulation results performed on plunge surface grinding process, discussed in the next chapter. Table 3.6 details these grinding conditions. Dressing conditions were selected based on the experiments performed for fine, medium and coarse dressing conditions as described earlier. Dressing conditions used in the experiments are listed in Table 3.7. Identical grinding conditions were applied to grind both AISI 1045 and AISI 52100 steels.

Table 3.6 Conditions for grind hardening experiments

Grinding Parameters	Values
Wheel Depth of Cut (mm)	0.025, 0.05, 0.1, 0.15
Feed Speed (m/min.)	0.25, 0.5, 1.0
Wheel Surface Speed (m/s)	25

3.3 Experimental Procedure

Straight surface plunge grinding experiments were conducted using the experimental setup illustrated in Figure 3.9. Grinding was carried out dry. Wheel speed was kept constant at 25 m/s. Wheel was freshly dressed after each experiment with the parameters mentioned in Table 3.7. Samples were than ground with grinding

Table 3.7 Wheel dressing parameters for grind hardening experiments.

Parameters	Value
Wheel Speed (m/s)	25
Dressing Depth (μm)	25.4
Transverse Feed Rate (m/min.)	0.5
Dressing Amount (mm)	0.130
Spark out passes	5

conditions listed in Table 3.6. 4 passes were taken for each specimen. Between each successive pass, there was a dwell of 5 to 10 seconds in order to stabilize the workpiece temperature.

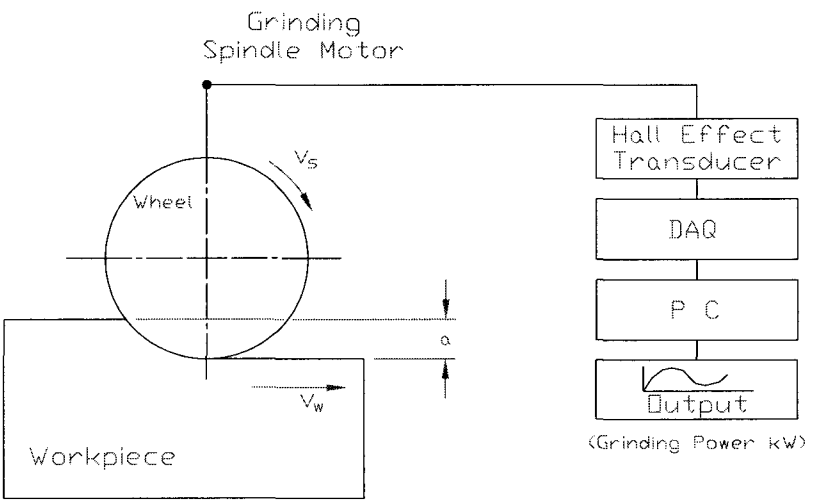

Figure 3.9 Schematic illustration of the experimental setup.

3.3.1 Grinding Power Measurement

The power consumed by three phase induction motors is measured as:

$$P = (E)(I)(Cos\theta)(1.73) \tag{3.3}$$

where

P = power (W),

I = current in each phase (A)

E = voltage (V)

Cosθ = power factor

1.73 is a multiplication factor, which is square root of 3 that refers to three phase. The power factor is a number, which tells to what extent the motor voltage and current are out of phase from one another. Common power factor ratings range from 0.78 to 0.98.

To measure grinding spindle power for the experiments, Hall Effect sensors were used as indicated previously. It senses the current provided to the grinding spindle motor and uses the voltage of the spindle motor as the sensor voltage. The device then multiplies the current and voltage. The resulting output is proportional to power. This is instantaneous vector multiplication which also calculates the lag or lead of the current (power factor). The signal for each of the three phases is summed and the analog output signal is proportional to the three phase power.

3.3.2 Metallurgical Analysis

Sample preparation

Preparation of metallurgical samples generally requires five major operations: sectioning, mounting (which is optional), grinding, polishing and etching. A well prepared metallurgical specimen is:

- Sectioned, ground and polished so as to minimize alterations caused by mechanical deformation, to allow the true microstructure to be revealed by etching.
- Free from polishing scratches, pits and liquid staining.

- Flat enough to permit examination at a high magnification using an optical microscope.

Specimens for case depth measurement were sectioned using a cutting saw and compression mounted using acrylic resins. The specimens were ground with the sequence involving abrasive grit of 150, 240, 400 and 600 mesh. They were then polished using 9, 3 and 1 micron diamond paste. Although some information may be obtained from as-polished specimens, the microstructure is usually visible only after etching. Only features which exhibit a significant difference in reflectivity (10% or greater) can be viewed without etching. Specimens were hence etched using 2% Nital solution.

Surface Hardness Analysis

Surface hardness was measured using a Rockwell superficial hardness tester. The Rockwell superficial hardness test method consists of indenting the test material with a diamond cone (N scale) or hardened steel ball indenter. The indenter is forced into the test material under a preliminary minor load F0 (Figure 3.10 A) usually 3 kgf. When equilibrium is reached, an additional major load is applied with resulting increase in penetration (Figure 3.10 B) while maintaining the preliminary minor load. When equilibrium is reached, the additional major load is removed but the preliminary minor load is still maintained. Removal of the additional major load allows a partial recovery, so reducing the depth of penetration (Figure 3.10 C). The permanent increase in depth of penetration, e, resulting from the application and removal of the additional major load is used to calculate the Rockwell superficial hardness number.

$$HR = E - e \tag{3.4}$$

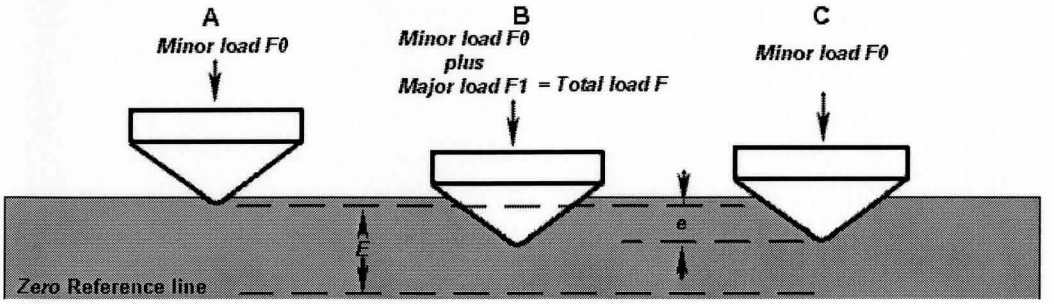

Figure 3.10 Principle of Rockwell hardness measurement.

Case Depth Analysis

Micro Vickers hardness is a measure of the hardness of a material, calculated from the size of an impression produced under load by a pyramid-shaped diamond indenter, whose opposite sides meet at the apex at an angle of 136°. The diamond indentor is pressed into the surface of the material at loads ranging up to approximately 1 kgf, and the size of the impression (usually no more than 0.5 mm) is measured with the aid of a calibrated microscope. The Vickers number (HV) is calculated using the following formula:

$$HV = 1.854\frac{F}{D^2} \tag{3.5}$$

Where F is the applied load (measured in kilograms-force) and D^2 is the area of the indentation (measured in square millimeters).

The case depth for the prepared specimen was measured in accordance with SAE standard J423-98 using an automated Vicker Hardness tester (Newage MS250-ASW) shown in Figure 3.11. This machine is capable of computerized case depth traverses with high speed motorized X/Y tables and automatic focus control for enhanced precision and speed. Indents were taken at intervals of 0.040 mm at a load of 300 g.

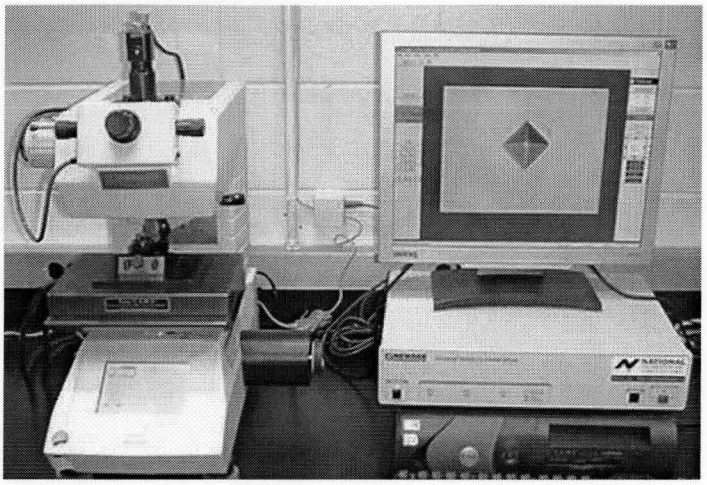

Figure 3.11 Automated micro vicker hardness tester.

In order to view the subsurface structure of the ground specimen, an optical stereo microscope (Nikon SMZ1000, capable of 50X to 200X magnification) was used. Based on the stereo microscope observation, selected specimens were observed in a scanning electron microscope (PHILIPS SEM515) for further examination of the microstructure.

Chapter 4

Results and Discussion

The material presented in this chapter consists of:

- A numerical thermal model formulation and analytical computations carried out to compute the temperature distribution beneath the ground surface to predict the incidence of surface hardening and the case depth.
- Experimental results exemplifying the effect of depth of cut, table feed and wheel topography on grind hardening. A discussion on power requirements for grind hardening is also included. Results of case depth and surface hardness analyses are presented to illustrate and characterize the grind hardening process and correlate them to the grinding conditions.

4.1 Numerical Modeling of Grind Hardening

The purpose of this phase of the study was to develop a finite element model of the plunge surface grinding process using a commercial software package to calculate the temperature field in the workpiece in order to understand the phase transformation of the work material during grinding.

Fundamentally, there are four variables in the analysis of phase transformation associated with grinding:

i. The strength and distribution of heat flux, which relates to the material removal mechanisms in grinding;

ii. The effect of convection which reflects the effect of coolant;

iii. The thermal properties of the work material, which determines the heat accumulation process, and

iv. The moving speed of the heat source, which represents the table speed in a plunge grinding operation.

In model simulations, particular attention was paid to the effects of heat flux and table speed with the following purposes:

- Determine critical heat flux values in order to attain workpiece temperatures above the Ac_3 line, and to examine its effect on the phase transformation, and
- Identify grinding conditions and threshold specific grinding energy that would enable achieving a set Effective Case Depth (ECD).

The work above was performed using a commercially available finite element analysis (FEA) software called DEFORM, which is especially designed to analyze various forming and heat treatment processes used by metal forming and heat treating industries. A key component of DEFORM is fully automatic, optimized remeshing system tailored towards large deformation problems. DEFORM-HT comprises the capability of modeling heat treatment processes, including normalizing, annealing, quenching, tempering, aging, and carburizing. DEFORM-HT can be used predict

hardness, residual stresses, quench deformation, phase transformation and other mechanical and material characteristics. DEFORM models the complex interaction between deformation, temperature, and, in the case of heat treatment, transformation and diffusion. There is coupling between all of the phenomenon, as illustrated in the Figure 4.1. The DEFORM system then solves time dependent non-linear problems

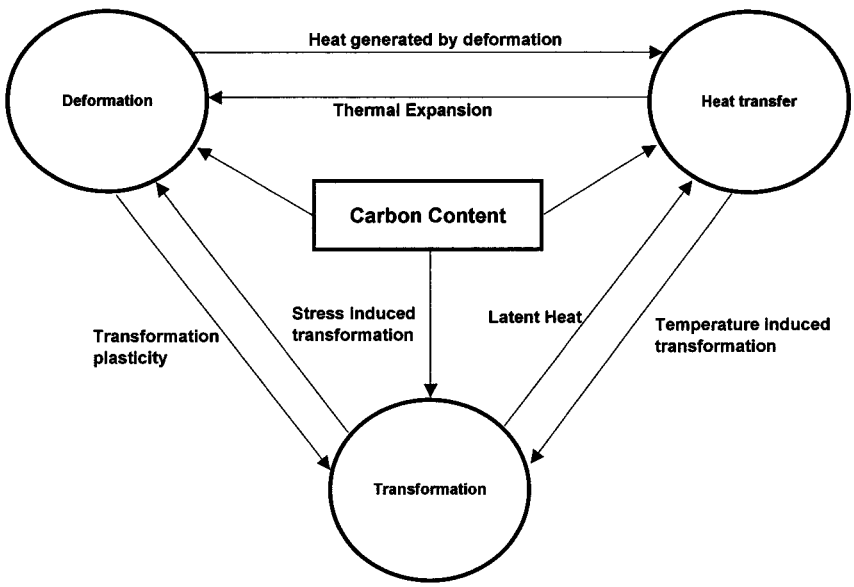

Figure 4.1 Relationship between various DEFORM modules [58].

by generating a series of FEM solutions at discrete time increments. At each time increment, the velocities, temperatures, and other key variables of each node in the finite element mesh are determined based on boundary conditions, thermo-mechanical properties of the workpiece materials and solutions at previous steps. Other state variables are derived from these key values and updated for each time increment. The length of the time step and number of steps simulated are determined based on the process simulated.

4.1.1 Model Parameters

Figure 4.2 shows a schematic representation of the plunge surface grinding process. A wheel that is rotating with a surface speed V_s is linearly traversed against the surface of a workpiece with a relative velocity V_w, at a depth of cut a, i.e. the depth of material removed during one pass of the wheel across the workpiece.

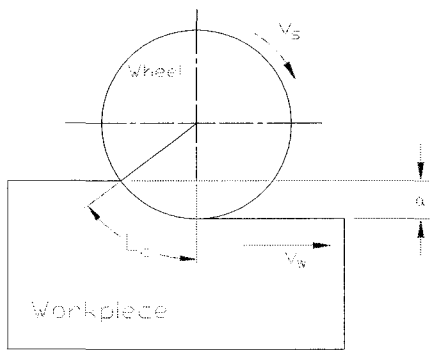

Figure 4.2 Plunge surface grinding geometry.

As a first step towards simulating the grinding process, temperatures produced by a moving heat source in a semi-infinite solid was analyzed. For this purpose a band heat source moving across the surface of a semi-infinite solid (workpiece) with a velocity V_w was considered. The basic simulation model on which the FEM-calculations were based is shown in Figure 4.3.

The grinding energy is considered to be dissipated over the rectangular grinding zone of length L_c along the arc of contact and width b. The grinding heat flux q entering the workpiece was assumed to be uniformly distributed over the grinding zone [28, 46]. Contact temperatures are primarily dependent on the average heat flux generated in the contact zone and the duration of heating. The distribution of the heat flux is of secondary importance [18]. Rowe et al. [18] calculated the surface temperatures for uniform heat flux and for a triangular flux distribution. He inferred that the maximum temperatures are not greatly different for the two flux distributions.

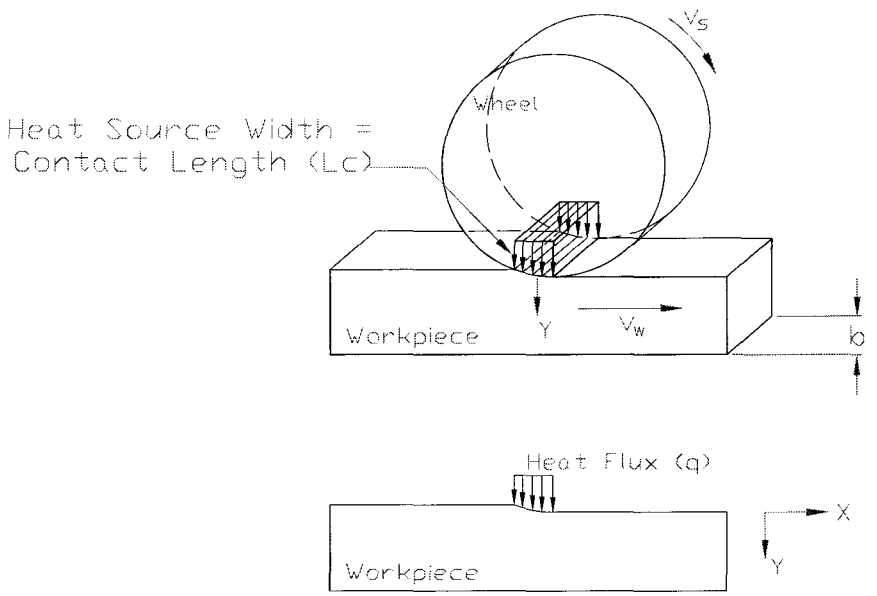

Figure 4.3 Two-dimensional model of the grinding process comprising a uniformly distributed heat source moving across the workpiece surface.

The main difference is the position of the maximum temperatures within the contact zone. For the uniform heat flux, the maximum temperature occurs at the trailing edge of the contact zone whereas for the triangular heat flux, the maximum temperature occurs at the midpoint of the band. Zhang et al. [59] performed an error analysis of the surface temperatures using finite element analysis, in comparison with analytical solutions available [21] for both rectangular and triangular heat flux distributions. He found that the maximum error is less than 6.5% for all grinding conditions considered.

The parameters, therefore established for the development of the FEA model are as follows:

i. 2-dimensional transient state uncoupled heat transfer.

ii. Temperature dependent material properties.

iii. Heat flux is applied on the work surface over a length equal to the geometric wheel-work contact length L_c and a width equal to the wheel width b.

iv. The geometrical and real contact lengths are assumed to be equal, and the geometrical contact area is assumed to be equal to the real contact area.

The analysis was conducted for AISI 1045 and AISI 52100 work materials. These materials are extensively used in general engineering applications and have good hardenability. AISI 1045 material has enough carbon content (0.45%) to transform to martensite when heated above the austenitic temperature and quenched at or below the critical cooling rate. AISI 52100 is an alloy steel and the alloying content in this material i.e. chromium, significantly reduces the critical cooling rate to form martensite. These characteristics, therefore make these materials suitable for grind hardening applications.

The thermal and metallurgical properties for these materials used in simulation are temperature dependent and were derived from the DEFORM material library. In order to simulate a heat treat process, inter-material data in the library defines the relationship between the transformation from one phase to another. This relationship is defined in terms of a kinetics model (in order to determine rate of phase transformation) and a few relational properties such as latent heat and volume change. Each phase is defined by its own set of material properties. These material properties define the plastic behavior, thermal properties and the elastic properties of the phase.

4.1.2 Boundary Conditions

Heat is dissipated into the workpiece at the grinding zone during grinding. Neglecting the deformation of both the grinding wheel and the workpiece, the geometric contact length (L_c) is simply taken equal to the arc length of the wheel in contact with the workpiece. Therefore,

$$L_c = \sqrt{aD_s} \tag{4.1}$$

where

D_s = wheel diameter

a = wheel depth of cut

The heat flux applied on the surface of the workpiece was varied from 2500 to 17500 W/mm^2. The purpose was to determine the critical heat flux values that correspond to grinding temperature above upper critical temperature line (Ac_3), to determine its effect on phase transformation at the workpiece subsurface. The basis for selecting this range was that the surface temperature, when calculated using an analytical technique [11] ranges from 200 to 1900 °C for typical table speeds.

The duration of heating time T_c during which the grinding wheel is in contact with the workpiece was calculated as:

$$T_c = \frac{L_c}{V_w} \tag{4.2}$$

The initial temperature of the workpiece was taken as the room temperature. The outside and bottom surfaces of the workpiece were modeled as insulated. The top surface was modeled to correspond to simple convection. The convective heat transfer coefficient h was constant for the top surface and was assumed to be 10 W/m^2 K. The simulation is insensitive to the specific value of h within the ranges appropriate for convection to air [60].Varying the value of h from 5 to 30 W/m^{2}K refer to less than 1% change in the maximum surface temperature.

4.1.3 Analysis and Simulation of the Grinding Process

FEA simulations were conducted with reference to two main process variables: (i) heat flux q and (ii) feed velocity V_w. The heat flux was varied from 2500 to 17500 W/mm^2 as indicated earlier, and the feed speed from 0.25 to 1.0 m/min. The reason for selecting such low feed speed was so that the Peclet number L selected for numerical simulation were in the range of $1 \leq L \leq 10$. The Peclet number L is interpreted as the ratio of the speed of the surface of the workpiece to the rate of diffusion of heat into it. At large values of L (typically greater than 10), the heat will diffuse only a short distance into the workpiece in the time taken for a point on the surface to move through the heated zone. The heat flow will then be approximately perpendicular to the surface at all points and solution tends to that for one-dimensional analysis. However, in the present study, a two-dimensional analysis was performed. The contact length L_c was taken as constant, which was 3.9 mm for all the simulations, calculated based on a depth of cut of 0.05 mm and a wheel diameter of 304.8 mm.

In the model developed, heat flux was applied on the top surface of the workpiece through a specified size window, the length of which was equal to the length of the grinding zone and a width equal to the width of the wheel width. This heat flux window was moved over the surface with velocity V_w of the workpiece. Another window called convection window was moved after the heat flux window through which the heat transfer convection coefficient was applied (Figure 4.4). It moved with a convection coefficient that corresponds to dry air, to simulate dry grinding. Figure 4.5 shows a typical temperature distribution in the workpiece owing to the heat flux moving over the workpiece surface.

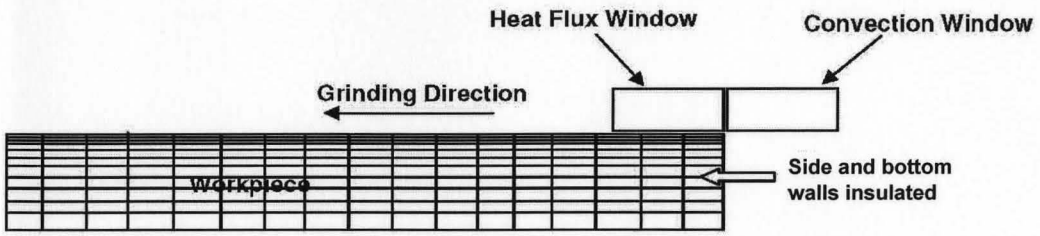

Figure 4.4 A schematic sketch of FEA model to simulate dry plunge surface grinding process.

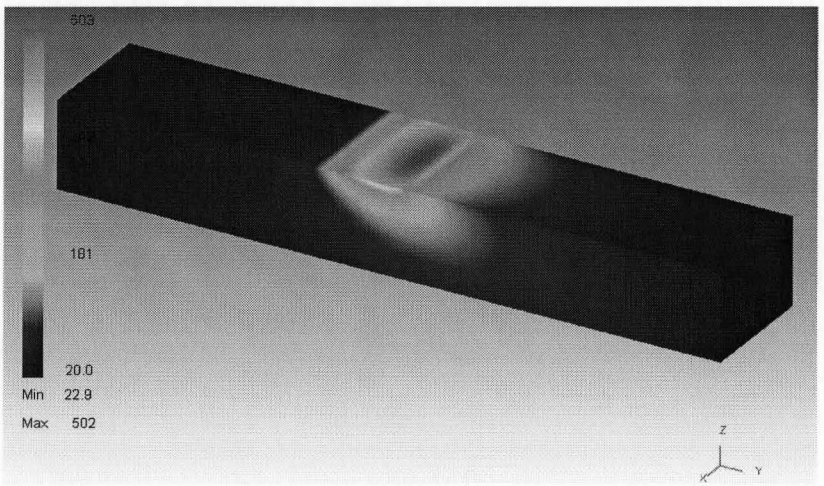

Figure 4.5 A typical temperature distribution in the workpiece owing to the heat flux moving over the workpiece surface.

4.1.4 Simulation Results and Discussion

Zhang et al. [59] used the finite element method to simulate the grinding process and studied the effect of table speed, heat flux distribution, thermal properties of work materials and convective features of the coolant. They established that the Peclet number L, convection heat transfer coefficient h and magnitude of heat flux q are the most important parameters that affect the grinding induced phase transformation.

They demonstrated that for a given L and q, martensite depth D decreases rapidly with the increase of h, i.e; a higher cooling rate produces a thinner martensite layer. This is because the phase transformation of a material needs time, i.e., to have phase transformation a time interval is required for changing the temperature to a critical level, but a larger h shortens such a time interval remarkably. They also emphasized that the Peclet number has a big effect on the process of phase transformation. For a larger L, and thus a larger feed speed, the phase transformation requires a higher heat input. In practice, the heat generated during grinding is a monotonic increasing function of the material removal rate. If the wheel depth of cut is constant, the heat generated would be the function of a feed speed only. For a large feed speed, the martensitic depth is usually much smaller. This is because a large L shortens the process of heat accumulation in the work material.

In the present study, the effect of magnitude of heat flux and table speed were simulated. To analyze the effect of these parameters, maximum surface temperature and effective case depth achieved during the simulation were examined. Effective case depth is defined as the distance measured along a line normal to the original surface of a hardened case to a point where the hardness first equals a specified hardness value. Maximum surface temperature was observed by increasing the magnitude of

heat flux q and decreasing feed speed V_w. At higher feed speeds the contact time between the heat source and the contact point of the workpiece surface is diminished and less quantities of heat penetrate into the workpiece due to lack of available time [2].

Martensitic phase transformation was observed for simulations where the surface temperature was close to 1000 °C. Higher transformation temperatures are due to the fact that during grinding, heating and cooling of the workpiece surface occur rapidly, which have an influence on manifesting phase changes in the surface. Van Vlack [61] derived an equation, described below to estimate mean surface temperature required during grinding to achieve phase transformation at a certain penetration depth.

$$\frac{\theta_y}{\theta_s} = 1 - \text{erf}(y/[2(\frac{k}{\rho C}T_c)^{0.5}]) \tag{4.3}$$

where

θ_y = mean temperature at a distance y below the surface

T_c = time of wheel-work contact

θ_s = mean surface temperature

erf = Gaussian error function

$\frac{k}{\rho C}$ = thermal diffusivity

From equilibrium phase diagrams [55] for AISI 1045 and AISI 52100, the temperature for the the ferrite-austenite transition is found to be 800 °C. The mean surface temperature required for martensitic depth of 0.25 mm can be calculated using Equation 4.3. Substituting the values $T_c = 0.168$ s ($V_w = 1.0$ m/min. and $L_c = 2.7$ mm), assumed temperature of θ_y of 800 °C, thermal diffusivity of 1.3×10^{-5} m^2/s for 1045 and 1.25×10^{-5} m^2/s for 52100 steel into Equation 4.3. Mean surface tem-

perature calculated for AISI 1045 and AISI 52100 were 986 and 990 °C respectively. This proves that higher surface temperatures are required for phase transformation during grinding.

Simulation results shown in Figures 4.6 and 4.7 indicated that at a feed speed of 1.0 m/min no phase transformation occurred even at higher heat flux quantities. As the feed speed is reduced to 0.5 and 0.25 m/min phase transformation start to occur at lower heat flux values. Maximum temperatures obtained for both the materials showed comparable results because of the similar thermal properties of the two steels. The maximum temperatures seen with feed speed of 0.25 m/s and heat flux quantities of 17500 W/mm^2 for 1045 and 52100 steels were 1940 and 1930 °C respectively. Effective case depth for AISI 1045 showed the same trend like that of AISI 52100 but the penetration depth is slightly shallower than that of 52100 steel. This is because of the fact that the critical cooling rate of AISI 1045 is much higher than that of AISI 52100.

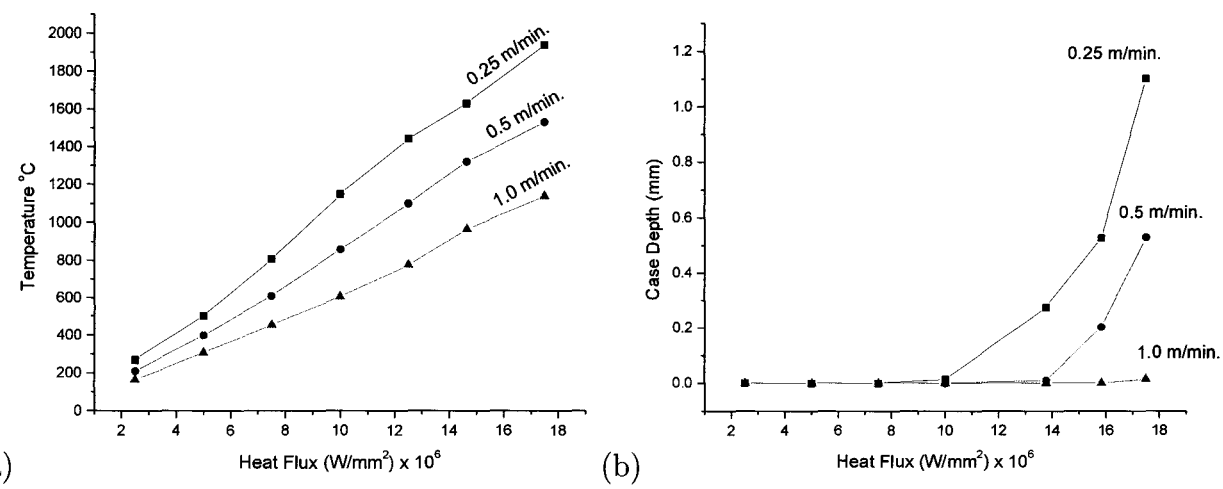

Figure 4.6 (a) Maximum surface temperature and (b) case depth at different values of heat flux and feed speed - AISI 52100.

Threshold values of heat flux and feed speed obtained from this simulation were

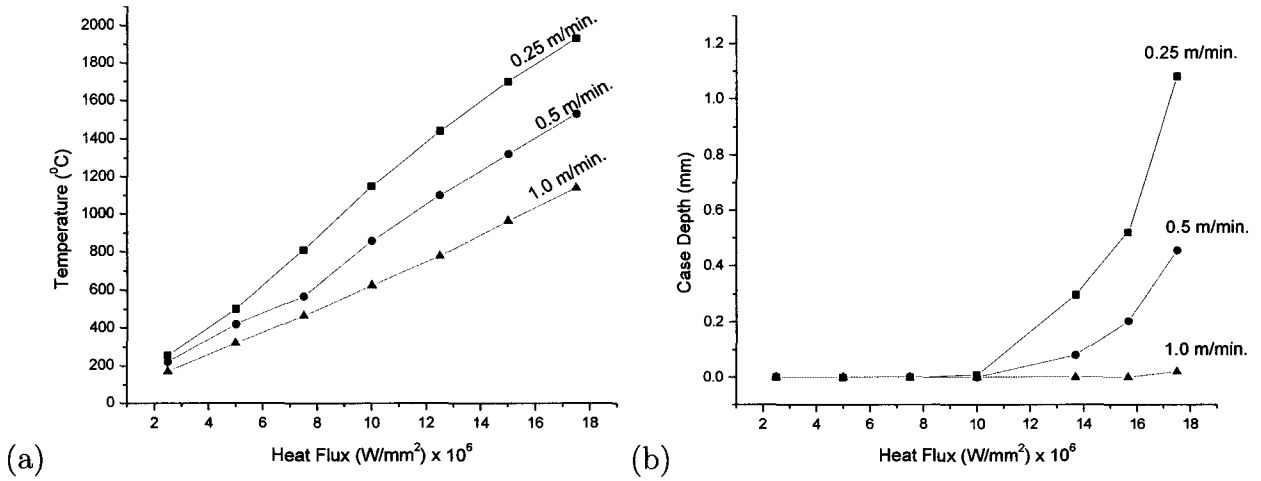

Figure 4.7 (a) Maximum surface temperature and (b) case depth at different values of heat flux and feed speed - AISI 1045.

used to calculate grinding power requirements and grinding specific energy. Grinding conditions where grind hardening to a certain depth can be achieved were established from the values of grinding specific energy.

4.1.5 Comparison of Numerical and Analytical Results

In order to verify the temperatures computed through FEA simulations, grinding temperature rise was also calculated analytically using a thermal model due to Malkin [11]. In this model, the heat flux is assumed to be uniformly distributed over the grinding zone, with the heated area likened to be a plane band source of heat, which moves along the surface of a semi-infinite solid (workpiece) at a velocity equal to the table speed. The maximum surface temperature T_m is given by:

$$T_m = \frac{1.13 q \alpha^{1/2} a^{1/4} D_s^{1/4}}{K V_w^{1/2}} \tag{4.4}$$

where

q = heat flux

α = thermal diffusivity

a = wheel depth of cut

D_s = wheel diameter

K = thermal conductivity

V_w = table speed

Temperatures obtained from Numerical modeling resulted in slightly higher values then those obtained from analytical solution (Figure 4.8). The maximum surface temperature variation estimated from analytical results to numerical results was limited to approximately 5% increase in temperature . This discrepancy could be due to thermal properties used in numerical modeling being temperature dependent while in the analytical solution temperature-independent properties have been used. Temperatures obtained from numerical simulations were therefore considered acceptable.

4.1.6 Power and Specific Energy Calculation

For given values of contact length and width of the workpiece, the grinding power was calculated for the values of heat flux used in simulation using equation 4.5.

$$q = \frac{R_w P}{L_c b} \tag{4.5}$$

Where R_w is the partition ratio, which is the proportion of the heat entering the workpiece to the total heat, P is the grinding power, L_c is the contact length and b is width of the workpiece. The purpose of calculating grinding power was to determine specific grinding energy as a function of material removal rate. From the calculated values of power and material removal rate, grinding specific energy u was calculated using equation 4.6.

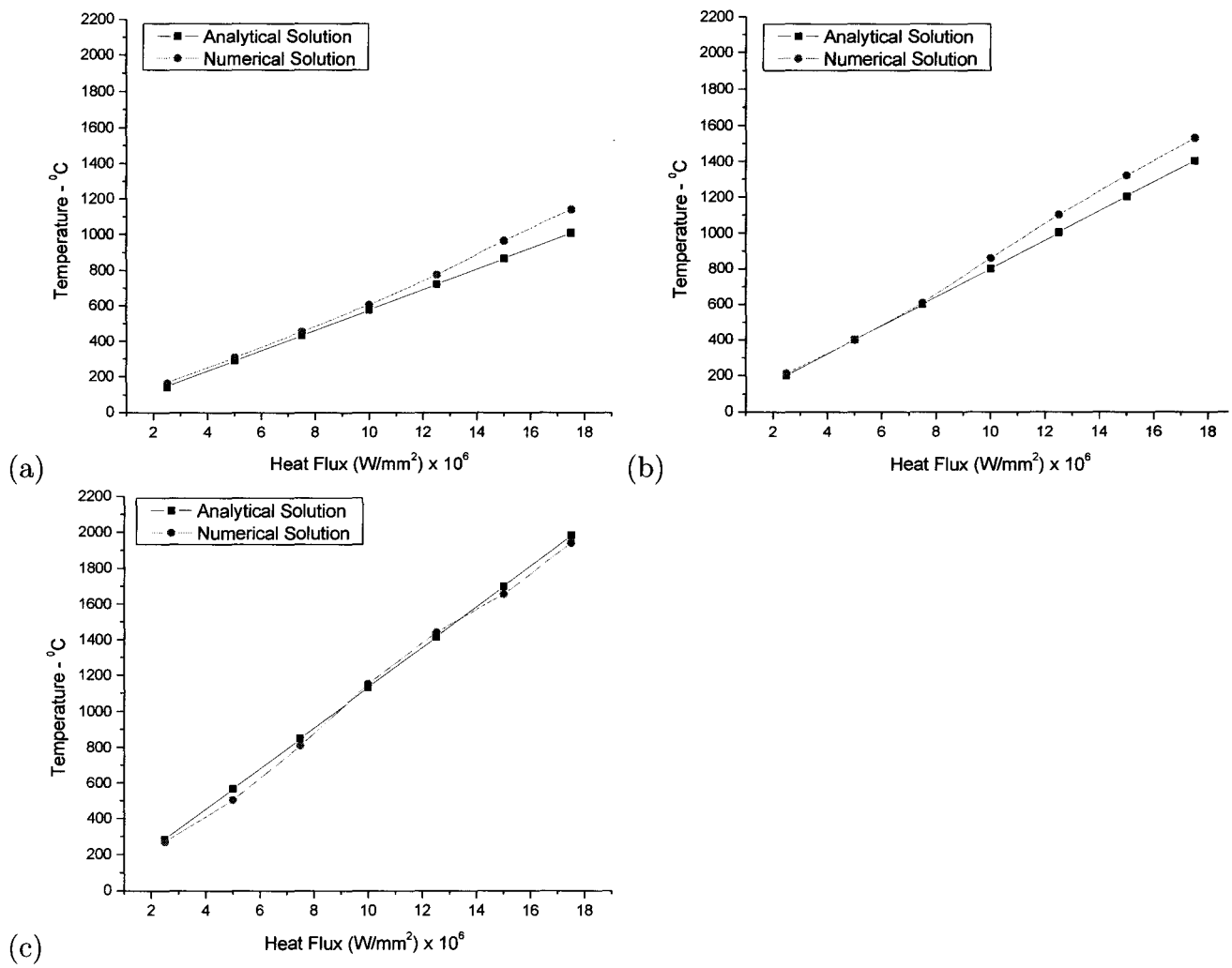

Figure 4.8 Comparison of maximum surface temperatures obtained from numerical and analytical models at a table feed of (a) 1 m/min. (b) 0.5 m/min. (c) 0.25 m/min.

$$u = \frac{P}{Q_w} = \frac{P}{V_w ab} \tag{4.6}$$

Specific grinding energy as a function of the material removal rate is plotted as shown in Figure 4.9. The domain separated into those where grind hardening was realized during simulations to those where there was no grind hardening. For those results where analysis showed grind hardening, there is general trend of decreasing specific energy as the material removal rate is increased. A polynomial is fit to indicate the hardening threshold in terms of the specific grinding energy required as a function of the material removal rate. This theoretical plot of grinding specific energy verses material removal rate can be used to determine required grinding spindle power to achieve grind hardening at certain material removal rate. Using this plot grinding conditions for the experiments were established, in order to validate this numerical model. These conditions are listed in Table 3.6.

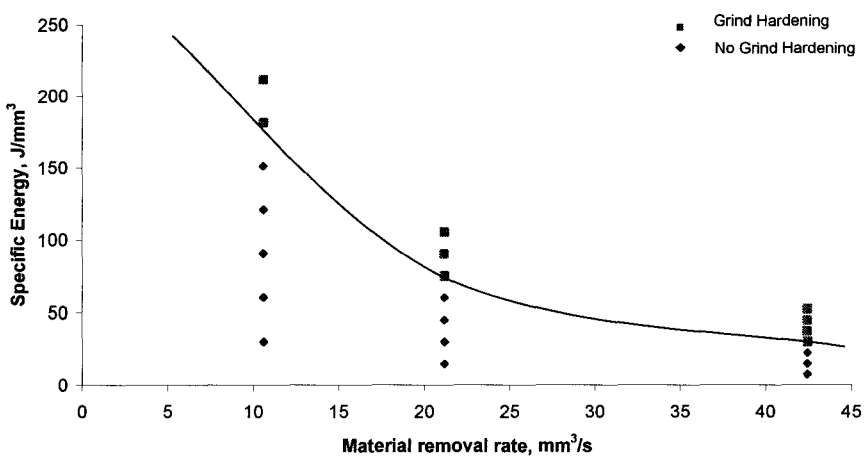

Figure 4.9 Hardening threshold in terms of specific energy and removal rate.

4.2 Grinding Tests

In order to validate the numerical model, grinding tests were performed for different depths of cut and feed speeds. 4 depths of cut (0.025, 0.05, 0.1 and 0.15 mm) and three feed speeds (0.25, 0.5 and 1.0 m/min) derived from the numerical model described in previous section were selected for these tests. Detailed grinding conditions are given in Table 3.6.

4.2.1 Effect of Wheel Depth of Cut

Fujii et al. [62] using Takazawa's approximation derived the following equation to calculate the maximum surface temperature rise θ_s as a function of work speed V_w, the depth of cut a and the wheel speed V_s:

$$\theta_s = 3.1 \frac{2R_w q\alpha}{\pi k V_w} \left(\frac{V_w L_c}{4\alpha}\right)^{0.53} \tag{4.7}$$

where

R_w = Partition ratio

q = Heat flux

α = Thermal diffusivity

V_w = Table feed

L_c = Contact length

k = thermal conductivity

They calculated maximum surface temperature at different wheel speed, table feed and depth of cut and validated it experimentally. They concluded that increasing depth of cut causes the greatest increase in surface temperature θ_s. e.g. the value of θ_s is 250 K for the depth of cut of 25 μm, and about 800 K for depth of cut of 80 μm.

In surface grinding with constant feed speed the depth of cut a is proportional to the specific material rate Q_w as well as to the equivalent chip thickness, so that increasing the depth of cut will result in higher process forces, almost in direct proportion (Figure 4.10). Because of increased grinding forces, grinding power is increased. The contact temperature therefore increases with increase in depth of cut.

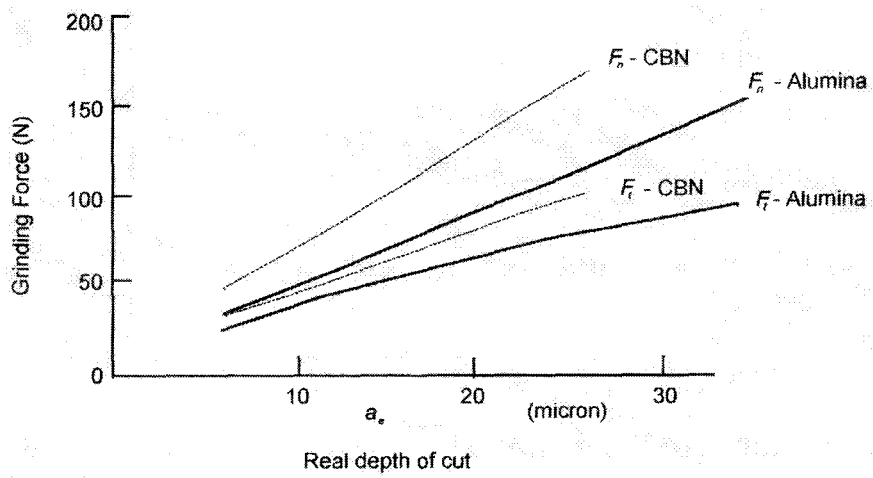

Figure 4.10 Grinding forces and depth of cut [18].

Brockhoff [3] also studied the effect of depth of cut on grind hardening and reported that the tangential forces increases with higher depths of cut. He reported specific energy, described in equation 4.8 is more appropriate to represent the resulting hardness profile. Specific energy shows a steady increase with increase in depth of cut because it leads to higher energy quantities entering into the workpiece.

$$e'' = R.P''.T_c \tag{4.8}$$

where R is the partition ratio, P'' is specific cutting power and T_c is the contact time.

Results of the present study also indicated a similar behavior as described above. Increasing the depth of cut resulted in increased hardened layer beneath the

surface. Increasing depth of cut will result in higher grinding forces, and increased grinding power (See Figure 4.11). Higher quantities of heat are therefore entering into the workpiece resulting in higher penetration depths. Figure 4.12 shows that there is no penetration depth at 0.025 mm depth of cut but penetration depth increases to 0.571 and 0.633 mm for AISI 1045 and AISI 52100 when the depth of cut is increased to 0.15 mm. 52100 steel shows higher penetration depth because of its better hardenability than 1045 steel.

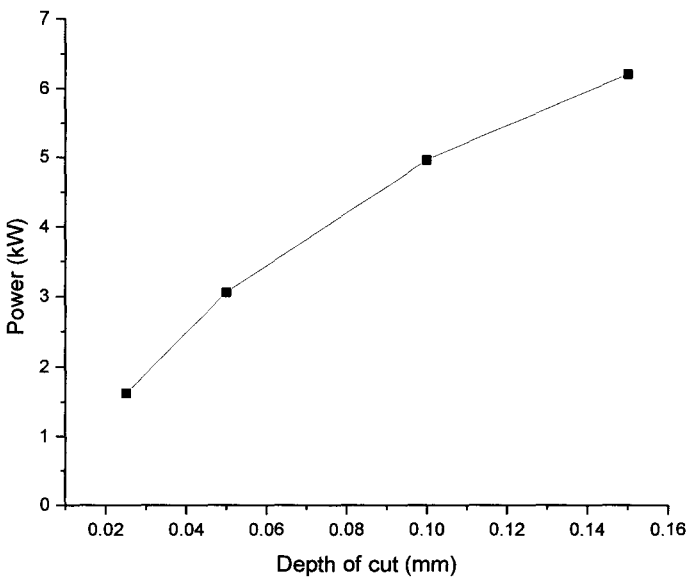

Figure 4.11 Maximum grinding power versus depth of cut.

4.2.2 Effect of Feed Speed

Brockhoff [3] studied the effect of feed speed on grind hardening. He reported that increasing feed speeds are generally connected with increasing process forces due to the higher material removal rate. Increasing tangential forces lead to a higher power consumption if all the other parameters are kept constant. High grinding power should generate higher temperature and increased hardened layer. But with increased

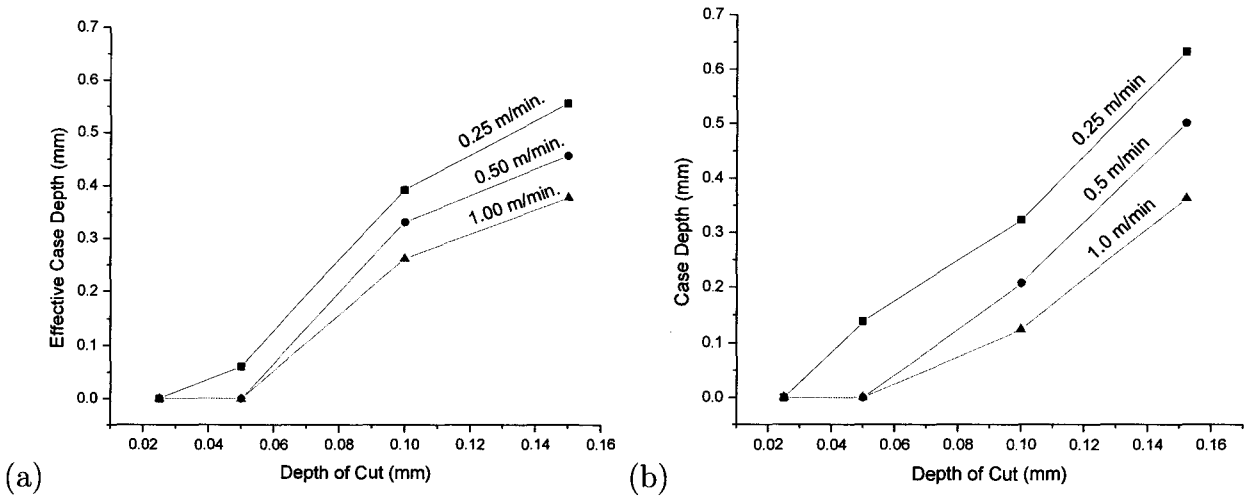

Figure 4.12 Effect of depth of cut and feed speed (a) AISI 1045 (b) AISI 52100.

table feed, the thickness of the hardened layer decreases. This decrease is caused by reduction in contact time between grinding wheel and fixed points of the workpiece. Therefore less heat quantities will penetrate into the workpiece due to lack of time. Brockhoff reported that medium feed speeds will result in maximum hardness penetration depth. At very low feed speeds the specific energy is high but due to lower supplied cutting power the extent of the hardened layer is reduced. At very high speed the cutting power increases, but due to the decreased contact time and lower traveling energy the extent of the hardened layer is again reduced. Hahn [23] used Jaeger's data for a moving band source in order to evaluate table feed behavior on temperature and yielded the plot shown in Figure 4.13. In this plot the relative temperature at the trailing edge of the source is plotted against the velocity ratio V_w/V_o. V_w is the table feed and V_o is an arbitrary reference speed. θ_o is the temperature at the trailing edge corresponding to the speed V_o. As an example, suppose a temperature of θ_o occurs at a table feed of 6 m/min. At 60 m/min. the temperature is 0.43θ and at 180 m/min. is 0.26θ. Hahn argued that this decrease in temperature is due to diminishing length of interference between the wheel and the workpiece with increasing work speed.

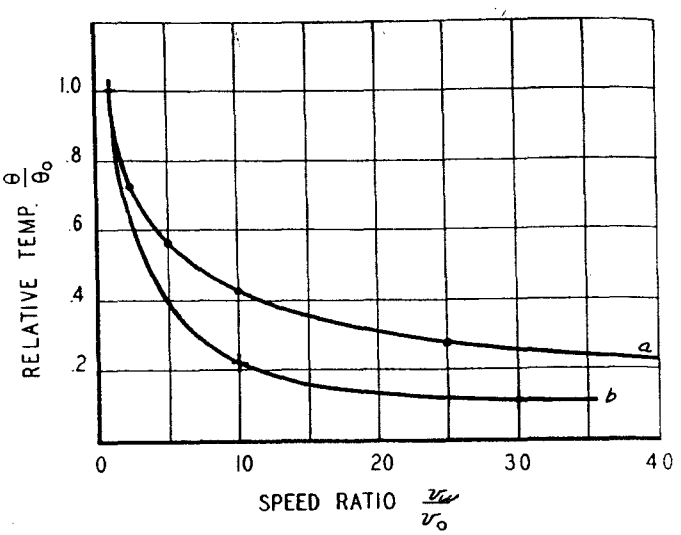

Figure 4.13 Illustration showing rapid fall in surface temperature as work speed increases [23].

In the present work, based on the information from literature and simulation results medium feed speeds were selected. Figure 4.12 shows that reducing feed speed result in increased penetration depth. When feed speed was reduced from 1.0 m/min to 0.25 m/min penetration depth increase from 0.36 mm to 0.64 mm for 52100 steel and from 0.37 to 0.56 mm incase of 1045 steel with depth of cut of 0.15 mm.

4.2.3 Effect of Wheel Topography

The topography of the grinding wheel is an important factor in the generation of heat required to surface harden the workpiece. In this phase of grinding tests, different wheel topographies were generated using different dressing conditions. Fine, medium and coarse dressing conditions were studied. These conditions are described in Table 3.5. Dressing is considered as a fracture process of the grains and bonds (Figure 4.14) as abundant cracks can be found in the grains and bond posts on the dressed wheel surface [57].

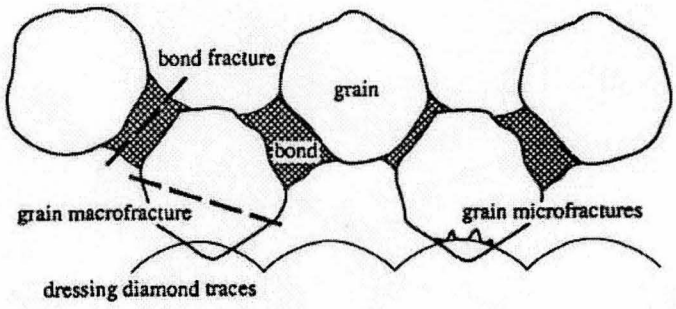

Figure 4.14 Grain fracture and bond fracture [57].

The topography of the wheel surface after dressing reflects the path of the dressing tool. The cutting edges of the wheel are shaped by the fracture and the plastic deformation of the grains. If the bond material is strong enough to withstand the dressing force, the dressing tool cuts through the grain, leaving relative large plateaus on the top of the grains. With finer dressing conditions, Malkin and Murray [63] observed a larger flattened area formed by plastic deformation on the top of the grains. Bhateja [64] suggested that dressing process consisted of gross fracture and levelling effects which may be explained by macro and micro processes. The macro action cleaves grains or breaks bonds giving the gross characteristics of the wheel working surface. The micro action refers to micro fractures of the grain surface.

Pande and Lal [65] showed that the proportion of bond fracture increases as dressing depth is increased or as dressing lead is decreased. The reason given was that increasing dressing depth increases the amount of wheel material removed during dressing, which produces a larger dressing force on the wheel and a higher probability of bond fractures. Decreasing the dressing lead increases the length of the dressing path on the wheel surface and increases the probability of bond fracture.

The shape of the dressing tool also effects the wheel topography. When a blunt dressing tool cuts through the wheel, the tops of the remaining grains are more flat.

As a consequence, the wheel is less sharp. The wheel sharpness depends on whether the prevailing effect of dressing is fracture or plastic deformation. Fracture makes the wheel sharp while plastic deformation makes the wheel blunt.

Results of the experiments are shown in Figure 4.15. It is inferred that power increases with decreasing dressing depth of cut 'a' and dressing lead 'f_d'. With fine dressing conditions, the number of active grains on the wheel surface is greatest, the grinding power therefore is high. With coarse dressing, whole grains are broken out of the surface, and the number of active grains on the surface is reduced. The grinding power is reduced after coarse dressing due to greater effective sharpness of the grains and due to the increased grain penetration.

Medium dressing conditions were therefore considered best for grind hardening since it produced enough power where an average effective case depth of 0.5 mm can be achieved with moderate grinding conditions.

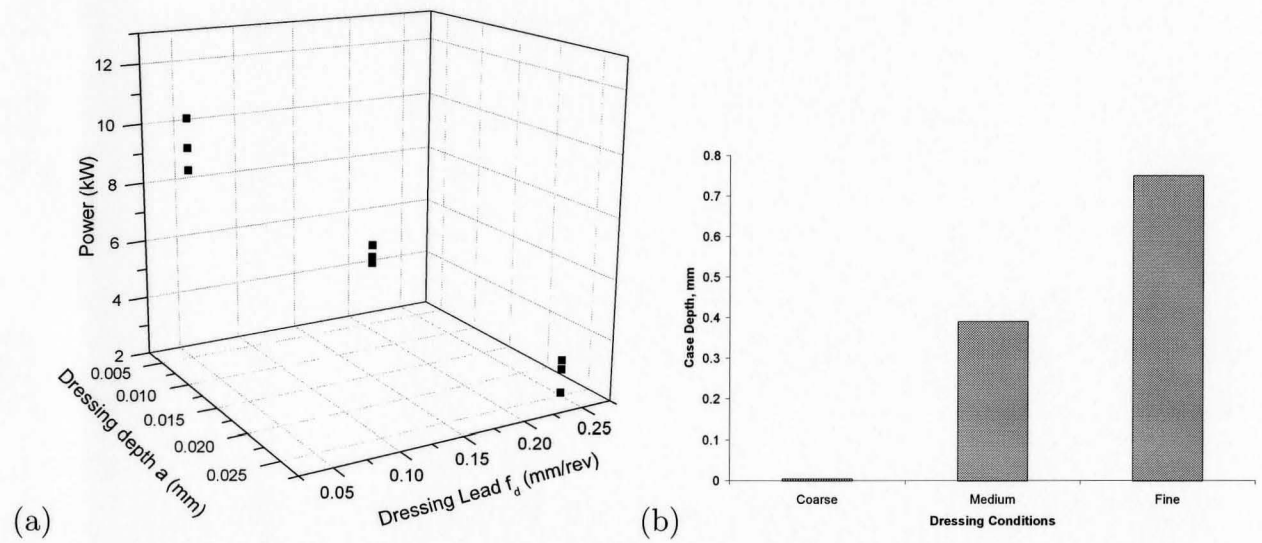

Figure 4.15 (a) Effect of dressing depth and dressing lead on grinding power (b) Effect of dressing conditions on case depth. (Material: AISI 1045, V_w = 0.5 m/min., a = 0.1 mm)

4.3 Metallurgical Analysis

A layer of material is transformed to martensite (α' phase) during grinding when a surface temperature reaches above upper critical temperature line. The important difference between this phenomenon called grind hardening and heat treatment of steels is that there is a very short time to allow carbon atoms to diffuse uniformly throughout the austenite (γ phase) to form martensite (α' phase) structure.

An important question to be answered is how than martensite can be obtained in grinding where the time at temperature is a small fraction of a second while it takes a much longer time in conventional heat treatment. The longer time required to form martensite in heat treatment is not due to ferrite-austenite transformation. The reaction time for ferrite to austenite is very small and is approximately 0.1 μs [66]. The longer time is due to decomposition of carbides and homogenization of carbon in austenite before quenching.

During grinding this time of decomposition of carbides is reduced because the material matrix (austenite) is not stationary as in heat treatment but is being plastically deformed at a very high rate during heating. Also, the transportation of carbon atoms in grinding is not only due to diffusion but is augmented by displacement of austenite relative to carbon atoms during plastic deformation [67]. The initial microstructure of the material plays an important role too, in decomposition of carbides and diffusion of carbon during austenitization.

The importance of retaining fine distribution of carbides in the initial microstructure for candidate materials which go through high heating rates and short austenitization cycles has been shown by Krauss [68]. He reported that this will result in more uniform diffusion of carbon in austenite phase and will result in extremely fine martensite, and higher hardness than produced by furnace heating [69]. The

fine distribution of carbides also induces microvoid coalescence, resulting in improved fracture properties [68].

Functional and metallurgical properties of the ground surfaces were therefore evaluated by measuring the surface hardness and effective case depth in accordance with SAE standard J423-98 and microstructural evaluation was conducted in accordance with ASTM standard A892-03.

4.3.1 Workpiece Surface Topography

During grind hardening the phase transformation (ferrite/perlite to martensite) causes volume increase which is hindered by bulk material resulting in compressive residual stresses [2] in the hardened layer. The compressive residual stresses hinders the initiation and propagation of micro-cracks resulting in improved fatigue life of the components.

In order to examine if ground surfaces were free from micro-cracks, grind hardened specimens were inspected using dye penetrat testing method. Surfaces were sprayed with red dye penetrant and left it to soak for one hour. Surfaces were then wiped off to remove excess penetrant and sprayed with developer (chalk). No crack was seen on any surface ground hardened at different grinding conditions.

4.3.2 Effective Case Depth

Polished and mounted specimens of AISI 1045 and AISI 52100 were inspected for effective case depth using automated micro hardness tester. Figure 4.16 and 4.17 present the effective case depth ground at 0.01 mm depth of cut. The target micro hardness to calculate effective case depth is taken at 513 HV, which is the expected hardness for plain/alloy steel after oil quench. Maximum hardness penetration depths

of 0.32 and 0.39 mm were seen for a depth of cut of 0.1 mm and a feed speed of 0.25 m/min. It is seen that the micro-hardness at the surface for both plain and alloy steel of the ground samples increased to HV_{300}=750, which is 3.5 times higher than that of the untreated steel.

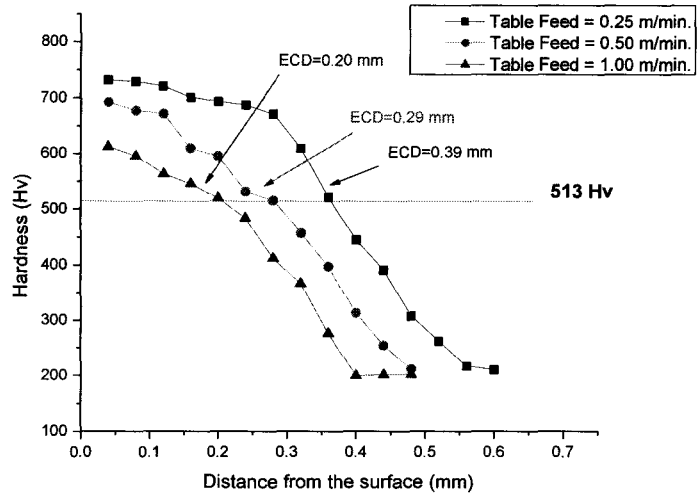

Figure 4.16 Vickers microhardness depth profile obtained from grind hardening experiment(Material: AISI 1045, V_s=25 m/sec, a=0.10mm).

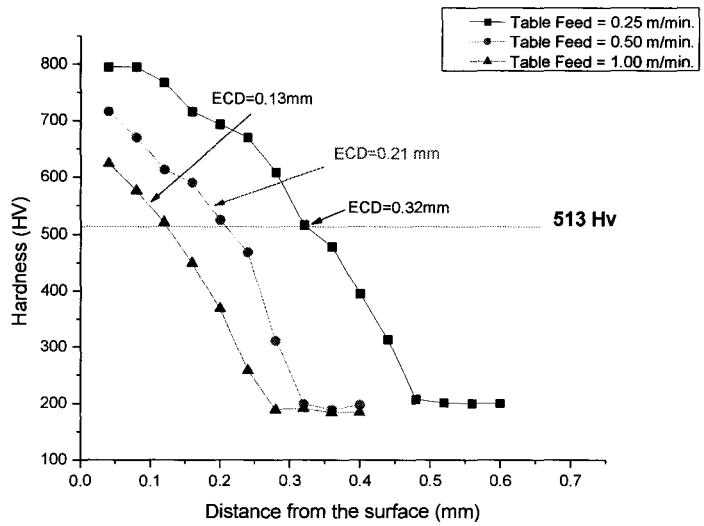

Figure 4.17 Vickers microhardness depth profile obtained from grind hardening experiment(Material: AISI 52100, V_s=25 m/sec, a=0.10mm).

4.3.3 Surface Hardness

Surface hardness was measured using a superficial Rockwell hardness tester. Surface hardness was seen increasing with increasing depth of cut. After reaching a value of HR 95 at 15 kgf, it leveled out. No further increase in hardness was observed by increasing depth of cut. This is the maximum surface hardness attained for 95% martensitic structure. Surface hardness verses depth of cut for 1045 and 52100 steels are shown in Figure 4.18.

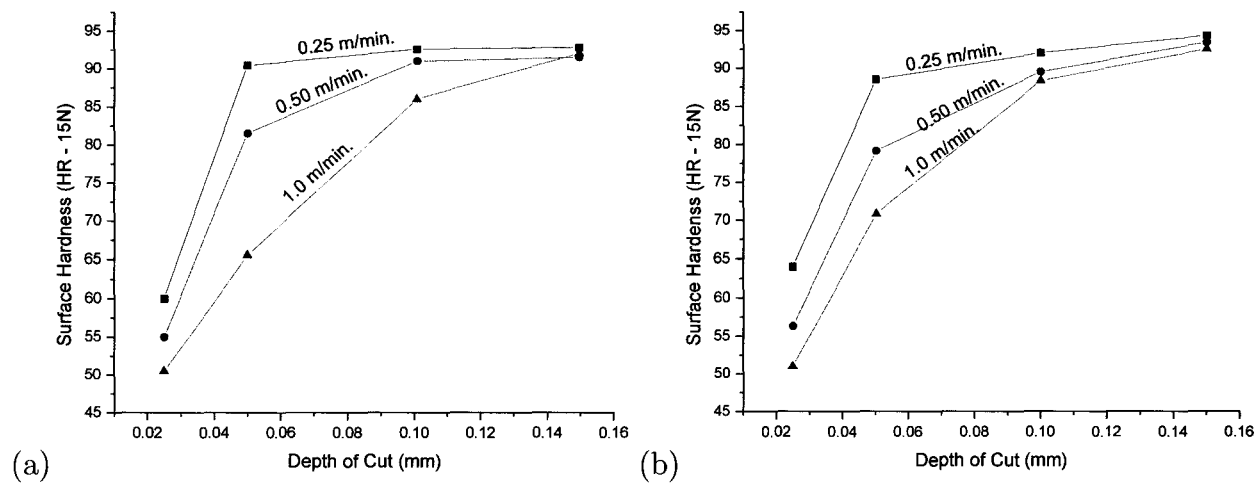

Figure 4.18 Surface hardness Vs depth of cut (a) AISI 1045 (b) AISI 52100.

4.3.4 Microstructural Evaluation

In order to examine phase transformation after grind hardening, micrographs of the subsurface were taken using optical and scanning electron microscopes. Microstructure were revealed by polishing and etching in a 2% nital solution. Both 1045 and 52100 steels showed short term austenitization and rapid quenching leading to martensitic structure at the surface. Sample cross-section were used in the analyses.

AISI 1045

The 1045 steel used in the experiment was initially annealed and tempered. Initial microstructures are shown in Figure 4.19. The microstructure shows white areas of proeutectoid ferrite and colonies of pearlite. Pearlite consists of very fine platelike or lamellar mixture of ferrite and cementite. The white ferritic background or matrix makes up most of the eutectoid mixture which contains thin plates of cementite. During grinding cementite in pearlite colonies in the vicinity of the area

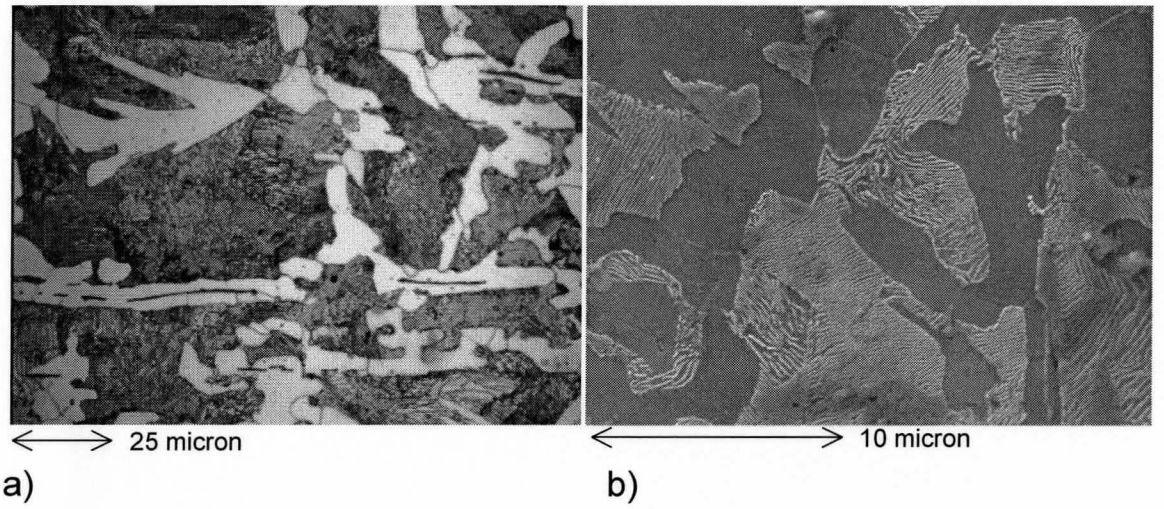

Figure 4.19 a) Optical, and b) electron micrographs of 0.45% carbon steel (1045). Pearlite colonies are visible in ferrite matrix

starts to dissolve at the Ac_3 point. Carbon atoms supplied from the dissolved cementite layer diffuse into the adjacent layer of ferrite and transforms the ferrite to austenite. When the heating rate is 10^4 K/s, pearlite dissolution requires only about 10 ms [70]. As the pearlite colonies are transformed to austenite, carbon atoms diffuse into the ferrite which surrounds the pearlite colonies and transforms ferrite to austenite. Transformed austenite is self-quenched due to the heat conduction into the surrounding region of steel. The austenite then starts the martensitic transformation at M_s temperature. Near the surface both the peak temperatures and diffusion time

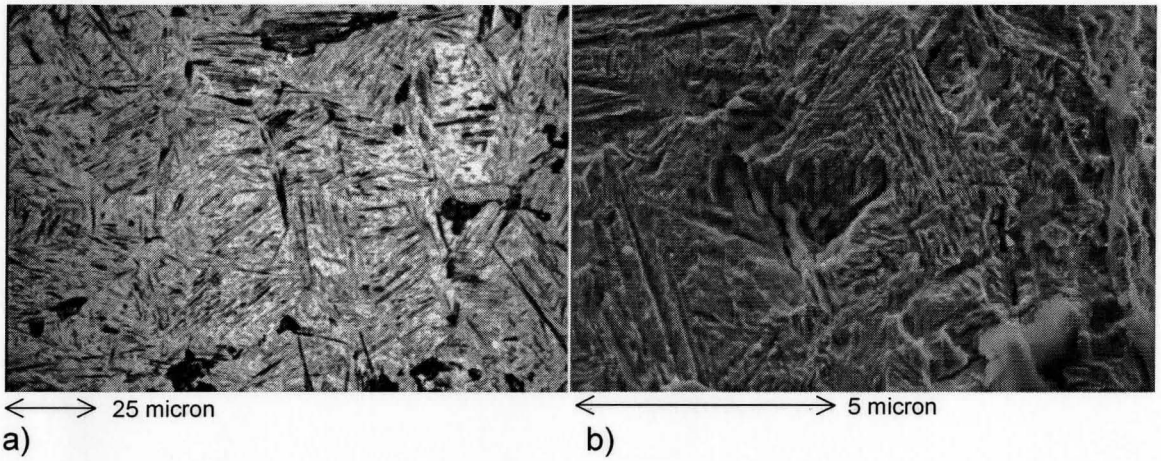

Figure 4.20 a) Optical, and b) electron micrographs of hardened layer of 1045 steel. Martensite structure shows plate-like laths.

are higher. As a result, low carbon austenite at the surface is transformed to martensite first and then higher-carbon austenite is transformed to martensite gradually. The optical microstructure of hardened layer (Figure 4.20a) shows a typical plate-like laths structure of martensite. Due to the material's carbon content (approx. 0.45%) the structure consist of acicular martensite that appears in the form of parallel needles within former austenite grains. This microstructure was further revealed using an electron microscope. It was observed that martensite laths were grouped in packets (Figure 4.20b). The martensitic laths inside packets were elongated in approximately the same direction in the average length of 3-5 μm and the average width was 0.3 -0.5 μm.

AISI 52100

The microstructure of AISI 52100 steel in the as received condition is shown in Figure 4.21. The microstructure shows fine spheroidized carbides (cementite) in a ferrite matrix. Microstructure does not show any retained carbide network or lamellar content. AISI 52100 is a high-carbon (1 percent) high-chromium (1.5 percent)

steel. When hypereutectoid steels are ground, the carbides in the ferrite matrix starts to dissolve when temperature reaches above A_{c3} line. Carbon atoms supplied from the dissolved cementite/carbide diffuse into ferrite matrix and transform ferrite into austenite. Martensite transformation starts at the M_s point when austenite is self quenched because of heat conduction into surrounding regions of steel. Figure 4.22a shows the micrograph of hardened layer. It shows nearly circular martensitic structure. Microstructure were further revealed using electron microscope (Figure 4.22b). These show fine and circular martensitic grains with a characteristic dimension of 0.3 -0.5 μm. The dislocation structure of the martensite fragments was mainly circular and no carbides were observed.

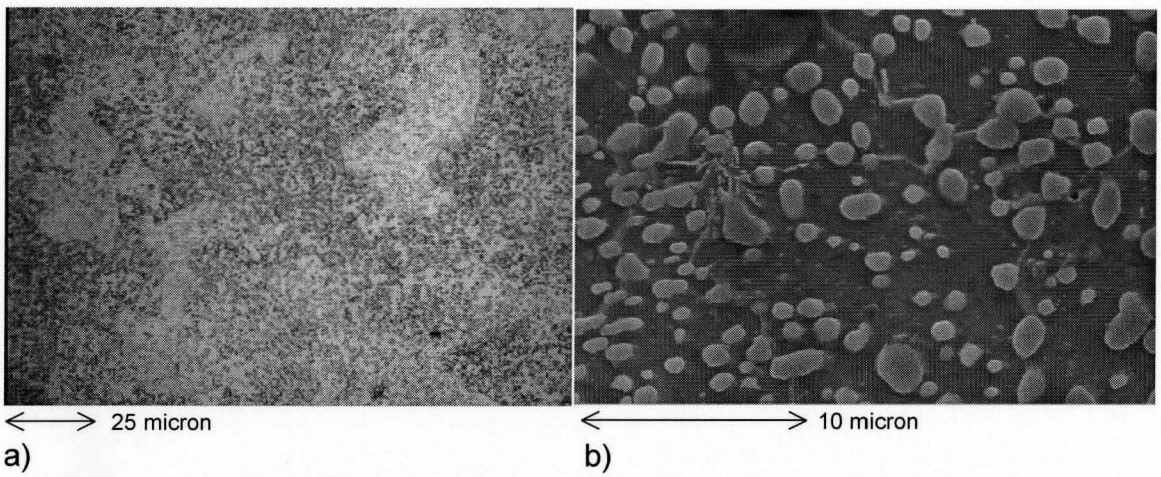

Figure 4.21 A 1 % carbon steel (52100) spheroidize-annealed, showing spheroidized cementite in a ferrite matrix. a) Optical, and b) Electron micrograph

4.4 Spindle Power Requirements

The measurement of grinding spindle power provides valuable information related to particular cutting process and the conditions that apply to the wheel and the machine tool settings. It is readily obtained since the power transducer is unobtrusive

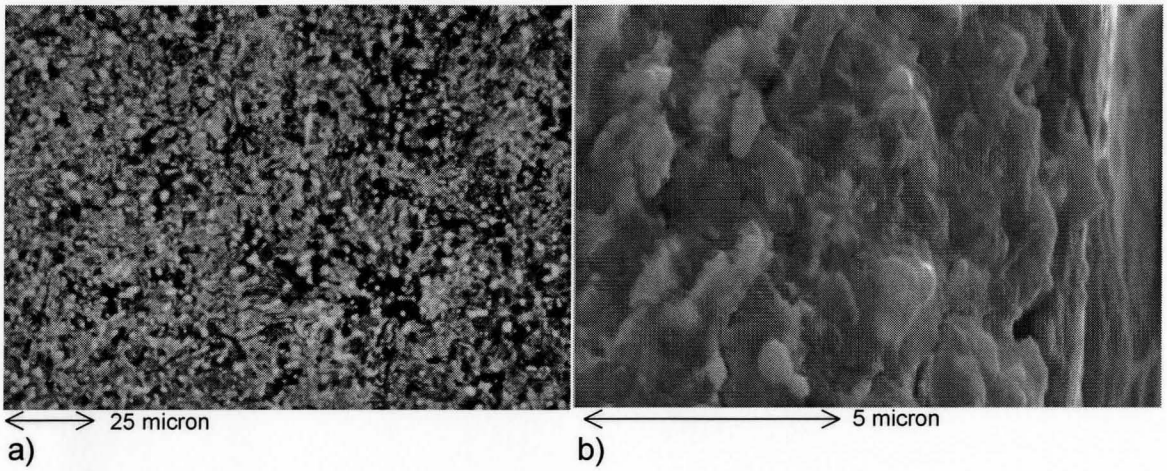

Figure 4.22 a) Optical b) electron micrograph of hardened layer of 52100 steel. Martensite structure shows fine and circular grains

and does not interfere with the grinding process.

In grinding processes, essentially all of the grinding power is dissipated as heat in the grinding zone, at the interface between the wheel and the workpiece [20]. Temperature prediction is based in most cases on measured power or grinding forces levels from which, the specific energy levels, can be determined. By monitoring the net grinding power, it can be readily determined in-process whether grind hardening is occurring.

In the present study, grinding power for each grind hardening experiment was measured in order to establish grinding power requirement where grind hardening can be achieved. The total grinding power at the wheel spindle was measured using Hall Effect Transducer from which the net power was obtained by subtracting the measured idle power. Figure 4.23 shows the relationship between case depth and the grinding spindle power. With the increase in grinding spindle power, more heat is dissipated into the workpiece, resulting in deeper martensitic phase transformation. It was observed that the minimum power required to achieve grind hardening is about 150 W/mm. As the spindle power goes up so does the case depth.

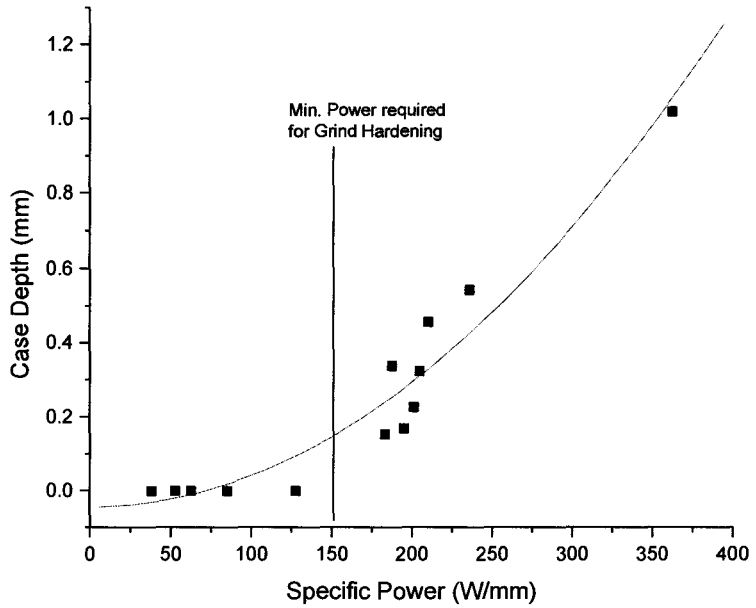

Figure 4.23 Hardening results depending on the grinding power.

4.5 Comparison of Experimental and Numerical Results

In order to compare grinding specific energies for experimental and numerical results, experimental points were plotted on Figure 4.10. Points are separated into those where grind hardening was measured to those where there was no grind hardening. A polynomial is then fit (Figure 4.24) along experimental points to show the hardening threshold in terms of the specific grinding energy required as a function of the material removal rate for experimental results.

Experimental and numerical values, although shows the same trend, values obtained experimentally are almost 50% more than numerical values. Reason for this difference is that the contact length used in numerical analyses is the geometrical contact length. Rowe et al [35], after reviewing the work of many researchers has reported that the actual contact length can be 50-200% greater then geometric contact

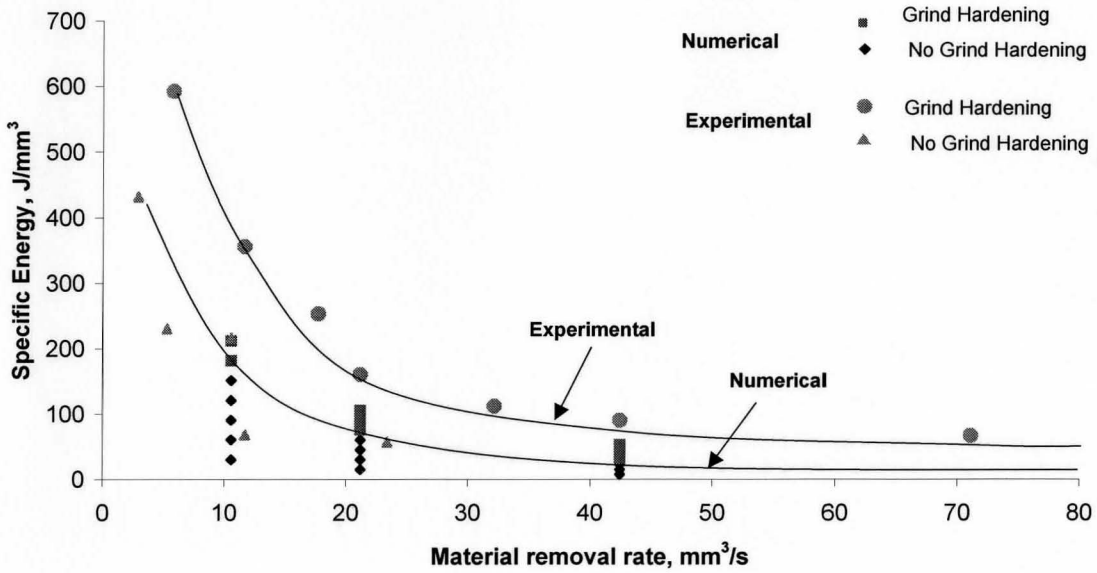

Figure 4.24 Comparison of grinding specific energy for experimental and numerical results.

length. Increased contact length causes the grinding spindle power to increase and ultimately, the specific grinding energy values are increased. This factor has caused the specific energy values obtained experimentally to differ from the values of numerical results.

This experimental plot of grinding specific energy verses material removal rate can be used to determine required grinding spindle power to achieve grind hardening at certain material removal rate. Therefore, using this plot grinding conditions that correspond to grind hardening to specified depths can be determined.

Chapter 5

Conclusions and Future Work

5.1 Conclusions

This paper presents the scientific basis and proof of concept for surface heat treating by grinding. Numerical and experimental investigations have shown that the generated heat in grinding could be effectively utilized as a new heat treatment process. The phenomenon was investigated on two different type of steels i.e. plain carbon and alloy steels. The main conclusions derived based on test results are as follow:

1. Grinding conditions (depth of cut and table feed), grinding wheel, workpiece material and wheel topography are the important factors affecting grind hardening

2. The grind hardened parts are characterized by fine plate-like martensitic structure, which were obtained by short-time austenisation of surface layers with self-quenching

3. Case depths up to 0.5 mm can be easily achieved with moderate grinding

conditions.

4. In order to achieve depths greater than 0.5 mm, higher depths of cut or slow table feed is required, which will lead to longer cycle times.

5. Wheel topography required to grind harden parts can be achieved using medium dressing conditions (a=0.015 mm and f_d=0.15 mm/rev).

6. Grind hardening can be used in a production environment without additional capital investment.

5.2 Suggested Work Flow for Grind Hardening

In order to achieve grind hardening at production level, the production flow shown the Figure 5.1 with following grinding conditions is proposed:

1. Rough grind the workpiece with depth of cut of 0.100 - 0.150 mm and feed speed of 0.25 0.50 m/min. No grinding coolant to be used during this operation

2. Measure power during grind hardening operation. Signals to be sent to dressing unit to dress the wheel when power value exceeds 400 W/mm.

3. Dress wheel with medium dressing (a=0.015 mm and f_d=0.15 mm/rev) conditions.

4. Institute online Eddy current tester in order to determine if grind hardening has occurred.

5. Finish Grind the workpiece using normal grinding conditions with coolant in order to attain the required form/finish tolerances

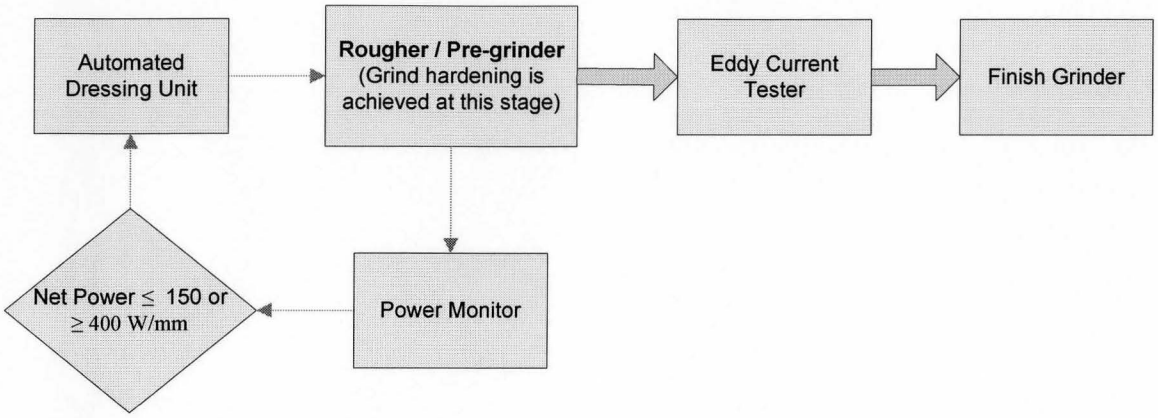

Figure 5.1 Purposed flow of grind hardening in a production environment.

5.3 Future Work

Suggestions for future work are described as below:

1. In order to adopt grind hardening technology by Niagara machine products, further experiments are required in order to duplicate technology on a centerless grinding machine.

2. More experiments are required in order to evaluate the robustness of the process.

Bibliography

[1] S. Malkin. Thermal aspects of grinding, part 2–surface temperatures and workpiece burn. *Journal of Engineering for Industry*, 96:1184–1191, 1974.

[2] E. Brinksmeier and T. Brockhoff. Utilization of grinding heat as new heat treatment process. *Annals of the CIRP*, 45(1):283–286, 1996.

[3] T. Brockhoff. Grind hardening: A comprehensive view. *Annals of the CIRP*, 48(1):255–260, 1999.

[4] D.C. Fricker, T.R.A. Pearce, and A.J.L. Harrison. Predicting the occurrence of grind hardening in cubic boron nitride grinding of crankshaft steel. *Journal of Engineering Manufacture*, 218:1339–1356, 2004.

[5] V.S.K Venkatachalapathy and B. Rajmohan. Experimental studies on the grind-hardening effects in cylindrical grinding. *Materials and Manufacturing Processes*, 18:245–259, 2003.

[6] H. Presell, C.R. Amend, and G. Gooch. Photothermal characterization of grind-hardened steel. *Review of Scientific Instruments*, 74:670–672, 2003.

[7] T. Nguyen, I. Zarudi, and L.C. Zhang. Grind hardening using liquid nitrogen. *International Journal of Machine Tools and Manufacture*, 47:97–106, 2007.

[8] L.P. Tarasov. Machining theory and practice. *ASM*, page 409, 1950.

[9] M. Field and J.F. Kahles. Review of surface integrity of machined components. *Annals of the CIRP*, 20(2):153, 1971.

[10] S. Malkin. *Grinding Technology: Theory and application of machining with abrasives.* Ellis Horwood Ltd., Chichester, 1989.

[11] S. Malkin. Burning limits for surface and cylindrical grinding of steels. *Annals of the CIRP*, 27(1):233–236, 1978.

[12] S. Malkin and C. Guo. Analytical and experimental investigation of burnout in creep feed grinding. *Annals of the CIRP*, 43(1):283–286, 0000.

[13] R. Soneys, M. Maris, and I. Peter. Thermally induced damage in grinding. *Annals of the CIRP*, 27(2):571–579, 1978.

[14] E. Brinksmeir, H.K. Tonshoff, and W. Konig. Residual stresses - measurement and causes in machining processes. *Annals of the CIRP*, 31(2):491–528, 1982.

[15] S. Malkin and O. Fedoseev. Analysis of tempering and rehardening for grinding of hardened steels. *Journal of Engineering for Industry*, 113:388–394, 1991.

[16] H. Eda, E. Ohmura, and S. Yamauchi. Computer visual simulation on structural changes of steel in grinding process and experimental verification. *Annals of the CIRP*, 42(1):389–392, 1993.

[17] M.C. Shaw and A.Vyas. Heat-affected zones in grinding steel. *Annals of the CIRP*, 43(1):279–282, 1994.

[18] D.M. Loan, W.B. Rowe, D. Boris, and I. Ichiro. *Tribology of Abrasive Machining Processes.* William Andrew Publishing, 1st edition, 2003.

[19] E.D. Doyle and S.K. Dean. An insight into grinding from a materials viewpoint. *Annals of the CIRP*, 29(2):571–575, 1980.

[20] O.J. Outwater and M.C. Shaw. Surface temperature in grinding. *Transactions of the ASME*, 74:73–81, 1952.

[21] H.S. Carslaw and J.C. Jaeger. *Conduction of heat in solids.* Oxford university press, Oxford, UK, 2nd edition edition, 1959.

[22] L. Blok. The surface temperatures under extreme lubricating conditions. *Second world Petroleum Congress, Paris, France*, pages 151–182, 1937.

[23] R.S. Hahn. The relation between grinding conditions and thermal damage in the workpiece. *Transactions of the ASME*, (78):807–812, 1956.

[24] R.S. Hahn. On the nature of grinding process. *Advances in Machine Tool Design and Research*, pages 128–154, 1963.

[25] S. Malkin and R.B. Anderson. Thermal aspects of grinding, part 1–energy partition. *Journal of Engineering for Industry*, 96:1177–1183, 1974.

[26] S. Ramanath and M.C. Shaw. Abrasive grain temperature at the beginning of a cut in fine grinding. *Journal of Engineering for Industry*, 110:15–18, 1988.

[27] H.K. Tonshoff, J. Peters, I. Inasaki, and T. Paul. Modeling and simulation of grinding process. *Annals of the CIRP*, 41(2):677–688, 1992.

[28] N.R. Des Ruisseaux and R.D. Zerkle. Thermal analysis of grinding process. *Journal of Engineering for Industry*, 92:428–434, 1970.

[29] R.S. Hahn. Thermal analysis of grinding process. *Journal of Engineering for Industry*, 92:433–434, 1970.

[30] N.R. Des Ruisseaux and R.D. Zerkle. Temperature in semi-infinite and cylindrical bodies subjected to moving heat sources and surface cooling. *Journal of Heat Transfer*, 92:456–464, 1970.

[31] D.Y. Gu and J.G. Wager. New evidence on the contact zone in grinding-contact length, sliding and cutting regions. *Annals of the CIRP*, 37(1):335–338, 1988.

[32] Z.X. Gu and C.A. Van Luttervelt. Real contact length between girning wheel and workpiece-a new concept and a new measuring method. *Annals of the CIRP*, 41(1):387–391, 1992.

[33] W.B. Rowe, M.N. Morgan, H.S. Qi, and H.W. Zheng. The effect of deformation on the contact area in grinding. *Annals of the CIRP*, 42(1):409–412, 1993.

[34] J. Verkerk. The real contact length in cylindrical plunge grinding. *Annals of the CIRP*, 24(1):259–264, 1975.

[35] W.B. Rowe, S.C.E. Black, B. Mills, K.N. Morgan, and H.S. Qi. Grinding temperatures and energy partitions. *Proc. Royal Society (London)*, 453(A):1083–1104, 1997.

[36] W.B. Rowe, S.C.E. Black, B. Mills, and H.S. Qi. Analysis of grinding temperatures by energy partitions. *Journal of Engineering Manufacture*, 210:579–586, 1996.

[37] J.F. Archard. The temperature of rubbing surfaces. *Wear*, 2:438–455, 1958.

[38] W.B. Rowe, J.A. Petit, A. Boyle, and J.L. Moruzzi. Avoidance of thermal damage in grinding and prediction of the damage threshold. *Annals of the CIRP*, 37(1):327–330, 1988.

[39] Y. Ju, T.N. Farris, and S. Chandrasekar. Theoretical analysis of heat partition and temperatures in grinding. *Journal of Tribology*, 120:789–794, 1998.

[40] A.S. Lavine. A simple model for convective cooling during the grinding process. *Journal of Engineering for Industry*, 110:1–6, 1988.

[41] A.S. Lavine and T.C. Jen. Thermal aspects of grinding: Heat transfer to workpiece, wheel and fluid. *Journal of Engineering for Industry*, 113:296–303, 1991.

[42] M.D. Demetriou and A.S. Lavine. Thermal aspects of grinding: the case of up grinding. *Journal of Manufacturing Science and Engineering*, 122:605–611, 2000.

[43] S. Kohli, C. Guo, and S. Malkin. Energy partition to the workpiece for grinding with aluminum oxide and cbn abrasive wheels. *Journal of Engineering for Industry*, 117:160–168, 1995.

[44] C. Guo and S. Malkin. Analysis of energy partition in grinding. *Journal of Engineering for Industry*, 117:55–61, 1995.

[45] T. Obikawa, O. Kakoki, and T. Shirakashi. Energy flowing rate into workpiece in surface grinding based on 3-dimensional temperature analysis–effect of measuring method on temperature distribution and energy flow rate. *International Journal of JSPE*, 32:19–24, 1998.

[46] S. Malkin and R.B. Anderson. Thermal aspects of grinding, part 2 – surface temperatures and workpiece burn. *Journal of Engineering for Industry*, 96:1177–1183, 1974.

[47] Z.B. Hou and R. Komanduri. On the mechanics of grinding process, part 2 – thermal analysis of fine grinding. *International Journal of Machine Tools and Manufacture*, 44:247–270, 2004.

[48] W.B. Rowe, S.C. Black, B. Mills, H.S. Ql, and M.N. Morgan. Experimental investigation of heat transfer in grinding. *Annals of the CIRP*, 44(1):329–332, 1995.

[49] T.D. Howes, K. Neaily, and A.J. Honsun. Fluid film boiling in shallow cut grinding. *Annals of the CIRP*, 36(1):223–226, 1987.

[50] W.B. Rowe, S.C. Black, B. Mills, and H.S. Qi. Analysis of grinding temperatures by energy partition. *Journal of Engineering Manufacture*, 210(B6):579–588, 1996.

[51] M.N. Morgan, W.B. Rowe, S.C.E. Black, and D.R. Allanson. Effective thermal properties of grinding wheels and grains. *Journal of Engineering Manufacture*, 212(B8):661–669, 1998.

[52] C. Guo and S. Malkin. Inverse heat transfer analysis of grinding, part 2:applications. *Journal of Materials Science*, 10:113–122, 1975.

[53] A.S. Lavine and S. Malkin. Thermal aspects of grinding with cbn abrasives. *Annals of the CIRP*, 38(1):557, 1989.

[54] I. Zarudi and L.C. Zhang. Mechanical property improvement of quenchable steel by grinding. *Journal of Material Science*, 37:3935–3943, 2002.

[55] ASM Handbook Committee. *Metals Handbook - Properties and Selection: Iron and Steels*, volume 4. American Society of Metals, Ohio, USA, 9th edition, 1999.

[56] J.L. Metzger. *Superabrasive Grinding.* William Andrew Publishing, 2003.

[57] W.B. Rowe, X. Chen, and M.N. Morgen. The identification of dressing strategies for optimal grinding wheel performance. *Proc. 30th Int. MATADOR Conf.*, 30:195–202, 1993.

[58] J. Fluhrer. *Deform 3D version 5.1 - User manual.* Scientific forming technologies corporation, Columbus, Ohio, 2004.

[59] L. Zhang and M. Mahdi. Applied mechanics in grinding - iv. the mechanism of grinding induced phase transformation. *International Journal of Machine Tools and Manufacture*, 35(10):1397–1409, 1994.

[60] L.K. Saunders. A finite element model of exit burrs for drilling of metals. *Finite Elements in Analysis and Design*, 40:139–158, 2003.

[61] V. Vlack. *Material Science for Engineers.* Addison Wesley, Massachusetts, 1970.

[62] T. Kato and H. Fujii. Temperature measurement of workpieces in conventional surface grinding. *Journal of Manufacturing Science and Engineering*, 122:297–303, 200.

[63] S. Malkin and T. Murray. Comparison of single point and rotary dressing of grinding wheels. *Proc. 5th North American Metalworking Research Conf.*, pages 278–283, 1977.

[64] C.P. Bhateja, A.W.J. Chisholm, and E.J. Pattinson. On the mechanism of diamond dressing of grinding wheel. *Proc. Int. Grinding Conf.*, 30:142–160, 1972.

[65] S.J. Pande and G.K. Lal. Effect of dressing on grinding wheel performance. *International Journal of Machine Tool Design and Research*, 19(3):171–179, 1979.

[66] Z. Nishiyama. *Martensitic transformation.* Academic Press, New York, 1978.

[67] M.C. Shaw. *Principles of Abrasive Processing.* Clarendon Press, Oxford, 1996.

[68] G. Krauss. Deformation and fracture in martensitic carbon steels tempered at low temperatures. *Metallurgical and Materials Transactions*, 32(A):861–877, 2001.

[69] G. Krauss. Martensitic microstructure and performance produced by bulk and induction hardening. *4th ASM Heat Treatment and Surface Engineering Conference; Florence, Italy*, pages 21–32, October 1988.

[70] E. Ohmura, K. Inoue, and K. Haruta. Computer simulation on structural changes of hypoeutectoid steel in laser transformation hardening process. *International Journal of JSME*, (1):32–45, 1989.